01 Jul 2023

Numerical Modeling Of Rock Blocks With Nonpersistent Rough Joints Subjected To Uniaxial Compressive And Shear Loadings

Mostafa Asadizadeh

Mahdi Moosavi

Mohammad Farouq Hossaini

Ahmadreza Hedayat

et. al. For a complete list of authors, see https://scholarsmine.mst.edu/min_nuceng_facwork/1715

Recommended Citation

M. Asadizadeh et al., "Numerical Modeling Of Rock Blocks With Nonpersistent Rough Joints Subjected To Uniaxial Compressive And Shear Loadings," *International Journal of Geomechanics*, vol. 23, no. 7, article no. 04023103, American Society of Civil Engineers, Jul 2023.
The definitive version is available at https://doi.org/10.1061/IJGNAI.GMENG-7858

Numerical Modeling of Rock Blocks with Nonpersistent Rough Joints Subjected to Uniaxial Compressive and Shear Loadings

Mostafa Asadizadeh[1]; Mahdi Moosavi[2]; Mohammad Farouq Hossaini[3]; Ahmadreza Hedayat[4]; Taghi Sherizadeh[5]; and Hossein Masoumi[6]

Abstract: Characterizing the mechanical behavior of jointed rocks is important to understand the behavior of structures in rock masses. Jointed rocks can be composed of persistent and nonpersistent joints where the impact of nonpersistent joints requires careful consideration for an accurate rock mass mechanical characterization. Most previous investigations into nonpersistent jointed rocks focused on joints with smooth surfaces, and a few experimental studies focused on nonpersistent rough joints and nothing specific has been reported numerically. Therefore, this study investigated several synthetic jointed rocks with nonpersistent rough joints numerically under uniaxial compressive and shear loadings. The PFC2D-based synthetic rock mass (SRM) approach was adopted to assess the impact of bridge angle (γ) and length (L), joint roughness coefficient (JRC), and normal stress (σ_n) on the shear strength (τ_n) and cracking in jointed rocks with nonpersistent rough joints. In addition, the impacts of γ, L, JRC, and joint inclination (θ) on the uniaxial compressive strength (UCS or σ_{cm}), elastic modulus (E_m), and failure pattern in the jointed blocks were examined numerically. First, several numerical models were developed and verified by the laboratory data, followed by an extensive parametric study to assess the effects of the defined parameters further. The effects of JRC and σ_n on τ_n were more pronounced than γ and L due to the formation of interlocking cracks, which could cause significant shear resistance during shear loading. In addition, the numerical results under axial loading revealed that an increase in θ could reduce the deformation modulus and the value of the other parameters, in particular the JRC, could lead to an increase in the strength of jointed samples.
DOI: 10.1061/IJGNAI.GMENG-7858.

Author keywords: Nonpersistent rough joint; Shear testing; Synthetic rock mass; Uniaxial compression.

Introduction

The role of discontinuities in the stability and failure of rock mass has been comprehensively studied by different researchers and practitioners in rock engineering (Brady and Brown 2004; Wittke 2014). These discontinuities might include joints, bedding, faults, and weak planes that, combined with intact rock, could form a complex rock mass structure. The discontinuities could appear in two forms: (1) persistent; and (2) nonpersistent. The initial investigations on the characterization of discontinuities were conducted by Patton (1966) and Barton (1976), who developed bilinear and nonlinear failure criteria for persistent joints, respectively. Then, a large number of studies were performed on the mechanical behavior of persistent joints experimentally (Brown and Trollope 1970; Einstein et al. 1969; Einstein and Hirschfeld 1973; Goldstein et al. 1966; Shaunik and Singh 2019; Singh et al. 2002) and numerically (Chang et al. 2019; Ma et al. 2018; Singh and Singh 2008; Wang et al. 2017; Zhao et al. 2016). Persistent joints have attracted significant attention; however, the critical role of nonpersistent joints in rock mass failure and their complex behavior under uniaxial compression (Asadizadeh et al. 2019b; Bobet 2000; Bobet and Einstein 1998; Park and Bobet 2009, 2010; Sagong and Bobet 2002; Tang et al. 2001; Wong and Einstein 2009; Wong and Chau 1998; Zhang and Wong 2013) and shearing have become evident from experimental studies (Amadei and Goodman 1981; Bahaaddini et al. 2014b, 2016b; Barton 1976; Grasselli 2006; Ivars et al. 2011; Jade and Sitharam 2003; Kovari et al. 1983; Lajtai 1969; Saeb and Amadei 1992; Xiong et al. 2020a, b), numerical investigations under uniaxial compressive loading (Bahaaddini et al. 2012, 2013b 2016a; Cao et al. 2016; Cheng et al. 2016a; Huang et al. 2019), and direct shear loading (Bahaaddini et al. 2013a, 2016b; Ghazvinian et al. 2012; Sarfarazi et al. 2017; Yang and Qiao 2018; Zare et al. 2021). Nonpersistent joints are impersistent or intermittent discontinuities (Wittke 2014). Understanding the degree of joint persistency could help rock engineers to design the structures better on or within the rock mass if the contribution of joints and intact rock to the overall mechanical behavior of the rock mass was known (Bahaaddini et al. 2016b; Cao et al. 2018; Shaunik and Singh 2019; Wang et al. 2019; Zhou and Chen 2019). A number of studies examined the mechanical behavior of jointed rocks with nonpersistent smooth joints (SJs) under uniaxial

[1]Colorado School of Mines, 1500 Illinois St., Golden, CO 80401 (corresponding author). ORCID: https://orcid.org/0000-0001-5944-0084. Email: masadizadeh@mines.edu

[2]School of Mining Engineering, College of Engineering, Univ. of Tehran, Tehran 1439957131, Iran. Email: mmoosavi@ut.ac.ir

[3]School of Mining Engineering, College of Engineering, Univ. of Tehran, Tehran 1439957131, Iran. Email: mfarogh@ut.ac.ir

[4]Colorado School of Mines, 1500 Illinois St., Golden, CO 80401. Email: hedayat@mines.edu

[5]Dept. of Mining and Explosives Engineering, Missouri Univ. of Science and Technology, Rolla, MO 65409. ORCID: https://orcid.org/0000-0002-6975-317X. Email: sherizadeh@mst.edu

[6]Dept. of Civil Engineering, Monash Univ., Melbourne, VIC 3800, Australia. ORCID: https://orcid.org/0000-0003-4993-1108. Email: hossein.masoumi@monash.edu

Note. This manuscript was submitted on March 24, 2022; approved on February 17, 2023; published online on May 12, 2023. Discussion period open until October 12, 2023; separate discussions must be submitted for individual papers. This paper is part of the ***International Journal of Geomechanics***, © ASCE, ISSN 1532-3641.

(a) (b) (c)

Fig. 1. Testing of (a) intact block and jointed artificial rock samples with persistent joint under; (b) uniaxial compressive; and (c) shear loadings.

compression (Afolagboye et al. 2017; Cao et al. 2015, 2020; Cheng et al. 2016b; Guo et al. 2020; Huang et al. 2016; Lee and Jeon 2011; Prudencio and Van Sint Jan 2007; Shaunik and Singh 2019; Wong and Chau 1998; Yang et al. 2020; Zhou et al. 2014) and shear loadings in a laboratory environment (Gehle and Kutter 2003; Ghazvinian et al. 2012; Lajtai 1969; Sarfarazi et al. 2014). A few experimental investigations included the nonpersistent rough joints under axial (Asadizadeh et al. 2018a, 2019a; Wong and Chau 1998) and shear loadings (Asadizadeh et al. 2018b; Fereshtenejad et al. 2021a, b) due to the complexities that are associated with the casting of synthetic rocks with rough joints.

Considering the roughness of joints in jointed rocks or rock masses with nonpersistent joints is important for most rock engineering projects because, in practice, the surface of joints is often rough with various roughness levels, which were described and categorized by Barton (1976) and based on the joint roughness coefficient (JRC). These joint roughness could have a favorable or adverse impact on the mechanical behavior of jointed rocks, where the former occur at high joint roughness, which could increase the joint's shear resistance. This could lead to the failure of a jointed rock at higher stresses, and the latter could refer to cases where there was little or no roughness and, therefore, easy shearing along the joint that could lead to rapid rock mass failure.

With the advances in computer technology and the development of different computational platforms for engineering problems, a new approach has opened for extensive mechanical investigations of complex rock mass behavior (Bahaaddini et al. 2013b, 2015, 2016a, b; Bahaaddini 2017; Park and Song 2009; Zare et al. 2021; Zhang and Wang 2020).

As highlighted previously, a few studies have experimentally investigated the mechanical behavior of rock mass with nonpersistent rough joints under uniaxial compression and shearing. To the best of the authors' knowledge, this study could be the first numerical attempt to investigate the mechanical behavior of jointed rocks with nonpersistent rough joints under uniaxial compressive and shear loading. The PFC2D that is based on synthetic rock mass (SRM) modeling is deployed to investigate the effect of a number of parameters, such as bridge angle (γ) and length (L), joint inclination (θ), JRC, and normal stress (σ_n) on the uniaxial compressive strength (UCS or σ_{cm}), elastic modulus (E_m), and shear strength (τ_n) of jointed rocks. In addition, the development of the failure pattern in jointed rocks with nonpersistent rough joints is assessed numerically. The models are initially calibrated with the experimental data reported by Asadizadeh et al. (2018b), followed by an extensive parametric study on the scenarios that were not experimentally explored. Furthermore, the cracking in a rock mass with nonpersistent rough joints is characterized by highlighting the crack initiation, propagation, and coalescence phases under uniaxial compression and shearing. Finally, the numerical results identify the important factors that contributed most to the macro fracturing process in jointed rocks with nonpersistent rough joints.

Parameter Determination and Calibration

The SRM technique, which is a combination of a bonded particle model (BPM) (Potyondy and Cundall 2004) and a discrete fracture network, was utilized to generate the jointed rock models (Bahaaddini et al. 2016a). In this technique, the joints were represented by the SJ (Dershowitz and Einstein 1988) and flat-jointed bonded particle models (FJ–BPM) as a disk–disk contact to simulate the behavior of a finite-length interface between both disks with local flat imaginary surfaces (Potyondy 2012). The intact material was modeled as an assembly of particles, which were bonded where the microproperties of the particles and bonds controlled the behavior of the intact assembly. The particles were unbreakable, and the bonds might break under tension or shear. Microcracks could be generated through the breakage of bonds in an FJ–BPM. The propagation and coalescence of microcracks could lead to the generation of macroscopic fractures. The problem of the overestimation of τ_n and the dilation angle in the removing bond method due to grain interlocking in a BPM could be overcome with the use of the SJ model (Pierce et al. 2007), in which the particles could overlap and pass through each other along the joint plane rather than moving around each other.

Physical Joint Parameters

To develop accurate numerical models, the measurement of some physical joint parameters was essential through a set of laboratory experiments. These parameters included the joint normal (k_n) and shear stiffness (k_s), and joint cohesion (c_j). Several uniaxial and shear tests were conducted on the slab-shaped artificial intact and jointed rock samples to estimate these parameters (Fig. 1). The samples were prepared and cast according to Asadizadeh

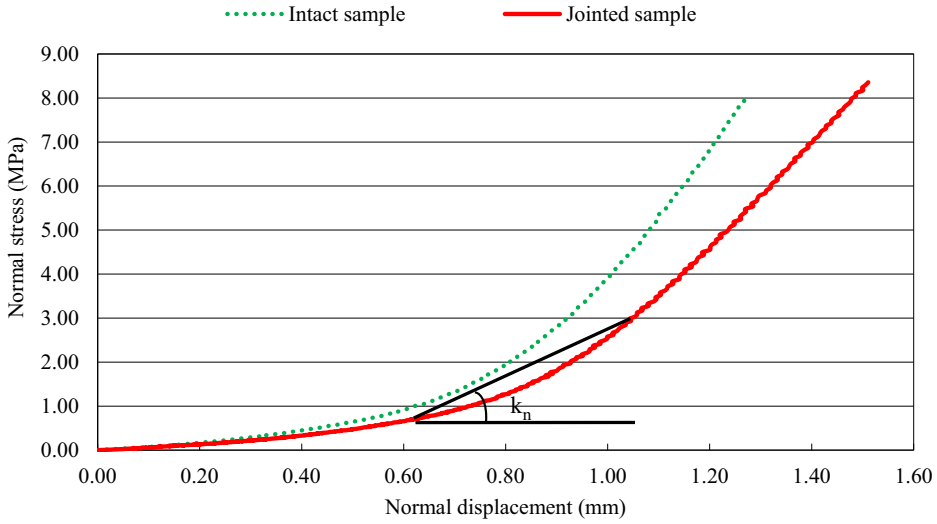

Fig. 2. σ_n versus normal displacement curve to calculate k_n in a jointed sample.

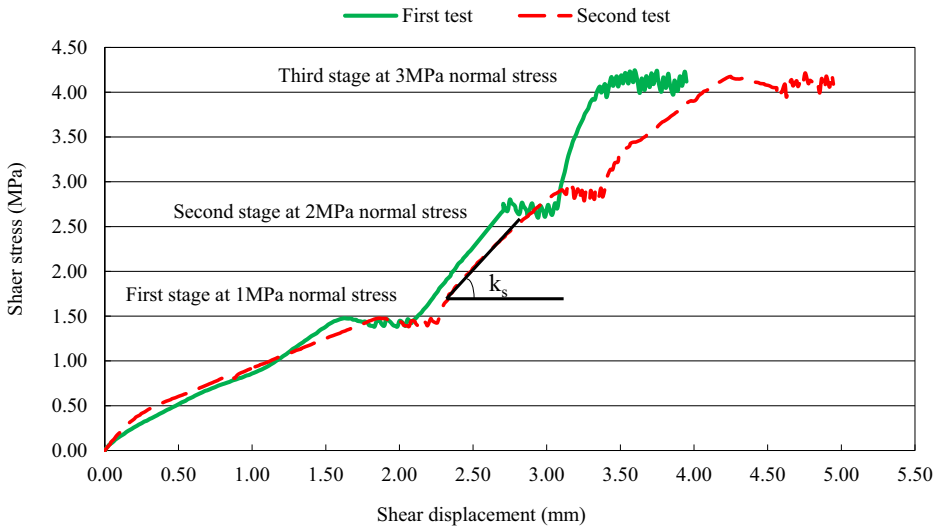

Fig. 3. Shear stress versus displacement curve of an artificial joint to calculate k_s and friction angle in jointed samples.

et al. (2018a, b 2019a) with $300 \times 300 \times 120$ mm^3 dimensions. The jointed samples included two intact blocks with contact through a persistent joint. One intact sample with half the size of a jointed rock sample ($300 \times 150 \times 120$ mm^3) was loaded axially to investigate its mechanical behavior under loading and unloading conditions [Fig. 1(a)]. Another jointed rock sample was subjected to axial loading normal to the joint orientation [Fig. 1(b)], and the last jointed sample was tested under direct shear where the loading was parallel to the joint direction [Fig. 1(c)]. A servo-controlled loading frame with a 400 t maximum loading capacity was utilized for the experiments. The novel shear box frame that was designed and fabricated by Asadizadeh et al. (2018b) was deployed for the shear test. The displacement rate for all the experiments was 5 μm/s, which was applied by Asadizadeh et al. (2018b).

Table 1. Results of laboratory experiments on the artificial jointed rocks under uniaxial compressive and shear loadings

Joint parameter	Value
Friction angle (°)	54.46
Cohesion (MPa)	0.00
System k_s (GPa/m)	1.20
System k_n (GPa/m)	4.50

The jointed sample with the persistent joint was loaded axially to approximately 8 MPa to obtain the σ_n versus axial displacement curve, as shown in Fig. 2. Therefore, the joint k_n was estimated as the secant (i.e., the slope of the linear section) of the σ_n versus axial displacement (Bahaaddini et al. 2013a; Bandis et al. 1983). The stress–displacement curve that resulted from the uniaxial compressive test on the intact artificial sample is shown in Fig. 2 for comparison with the curve that was attained from the jointed sample.

The k_s and joint friction angle were obtained from two multistage direct shear tests on the jointed sample shown in Fig. 1(c). The tests were conducted according to the International Society for Rock Mechanics (ISRM) suggested method (Muralha et al. 2014). A sample was subjected to direct shear loading when the constant σ_n was varied at different stages. In this study, three different σ_n that included 1, 2, and 3 MPa were selected for these experiments, and the shear stress–shear displacement data were recorded during the shear loadings (Fig. 3).

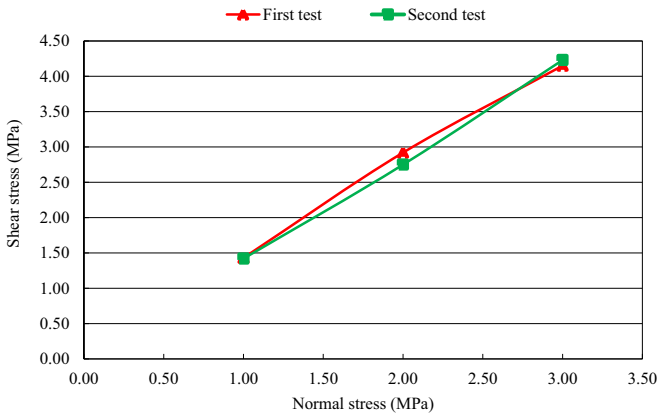

Fig. 4. Shear stress versus σ_n curve obtained from multistage shear tests on jointed samples.

Therefore, k_s was calculated for each stage of loading, which was the slope of the linear zone. Then, the average of two tests was represented as the k_s of the created joints (Table 1).

The friction angle of a joint was calculated using the Mohr–Coulomb criterion from the shear stress versus σ_n data (Fig. 4). The friction angles of 54.29° and 54.63° were estimated for the first and second tests, respectively. Therefore, their average was defined as the friction angle of the joint for numerical modeling. Due to the lack of cohesion during joint fabrication, $c_j = \text{zero}$.

Calibration of FJ–BPM and SJ Microparameters

The estimation of the microproperties of the particles, bonds, and SJ was not feasible through laboratory experiments. Therefore, a trial and error process that was inspired by the uniaxial compressive and Brazilian tests (Bahaaddini et al. 2013b; Itasca Consulting Group 2022; Sarfarazi et al. 2014; Mehrdad et al. 2022) was used. First, the macroproperties were measured, and then the microproperties were back-calculated using trial and error.

Table 2. Calibrated microparameters of FJ–BPM

Parameter	Value
Balls	
Density (kg/m^3)	1,610
R_{min} (mm)	0.30
R_{max}/R_{min}	1.67
tan ϕ_j	0.50
k_n/k_s	2.42
FJ–BPM	
$\bar{\lambda}$	1.00
$\bar{E}_c$ (GPa)	3.16
fjm_pb_ten (MPa)	5.50
fjm_pb_coh (MPa)	8.50
fjm_pb_fa	1.224
$\bar{k}_n/\bar{k}_s$	2.42

FJ–BPM Calibration

The microscale properties of a BPM were commonly calibrated against σ_{cm}, Young's modulus (E), and Poisson's ratio (ν) (Bahaaddini et al. 2013a; Potyondy and Cundall 2004), which were obtained from the uniaxial compressive experiment. First, a number of parameters were calibrated that included E, which was dependent on the particle modulus (E_c), the parallel bond modulus ($\bar{E}_c$), the particle k_n to k_s ratio (k_n/k_s), and the parallel bond k_n to k_s ratio ($\bar{k}_n/\bar{k}_s$). Then, in an iterative process, ν was calibrated, which was dependent on the ratios of k_n/k_s and $\bar{k}_n/\bar{k}_s$. Therefore, the σ_{cm} was calibrated, which was controlled by the k_n and τ_n of the parallel bonds (Bahaaddini et al. 2013b; Potyondy and Cundall 2004). Finally, the tensile strength (σ_t) of a numerical sample was calibrated based on the data that were obtained from the Brazilian test. This led to the microparameters listed in Table 2.

As given in Table 2, the maximum circle's radius was R_{max}, and the minimum circle's radius was R_{min}, which could be defined based on the joint roughness profile, and the ratio of R_{max} to R_{min} could create the joint roughness profile. Then, k_n/k_s was the ratio of k_n to k_s of the ball contacts, the radius multiplier was $\bar{\lambda}$, and the E_m of the FJ band was $\bar{E}_c$. In addition, fjm_pb_ten, fjm_pb_coh,

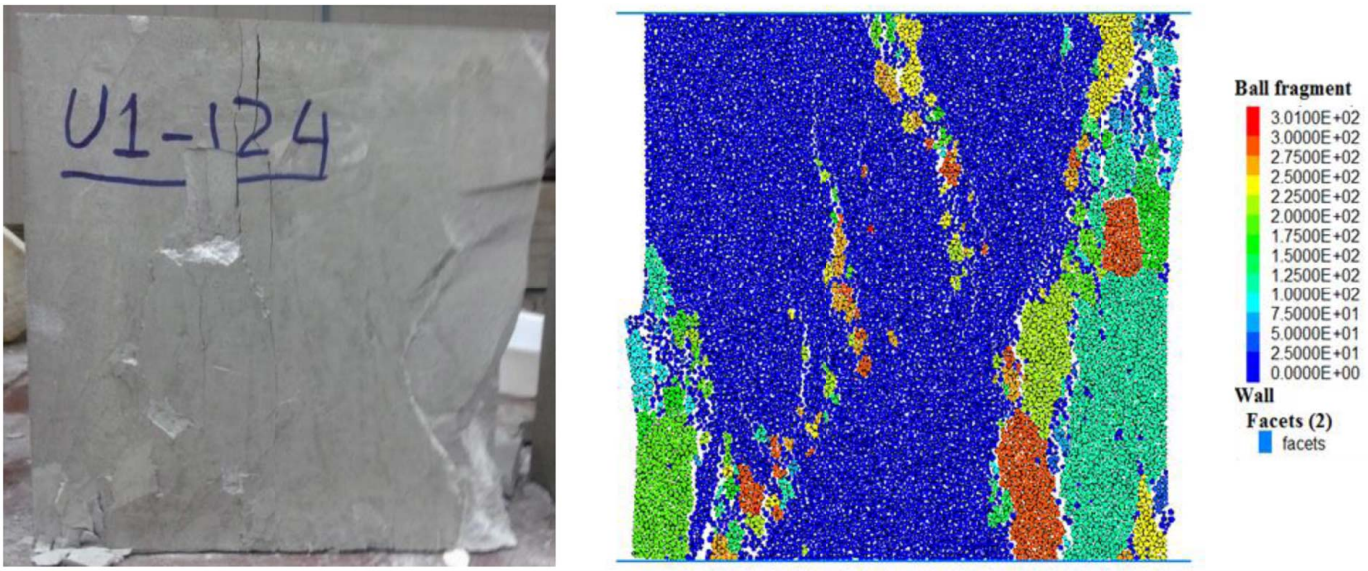

(a) (b)

Fig. 5. Comparison of failure patterns that were obtained from uniaxial compression under (a) laboratory environment; and (b) numerical simulation.

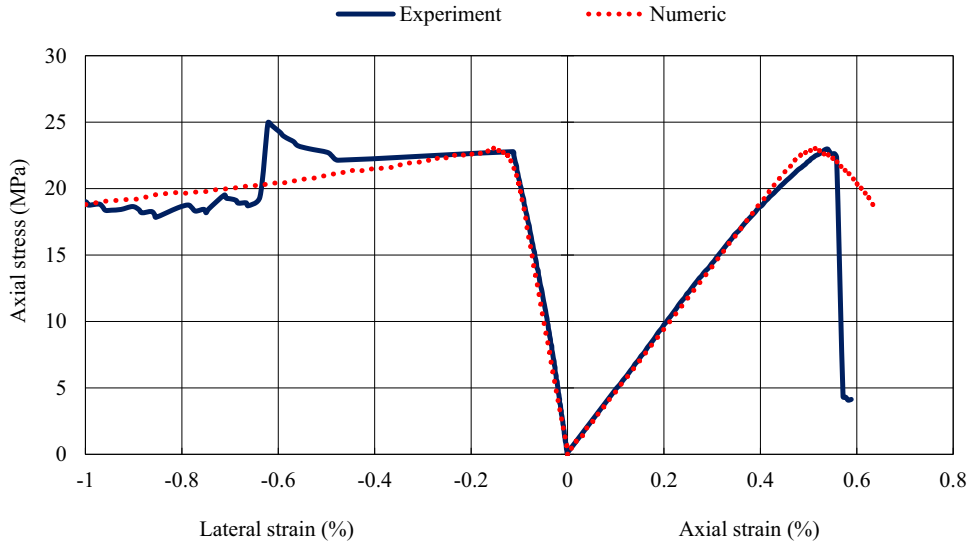

Fig. 6. Comparison of stress–strain curves that were obtained from experimental and numerical simulations under uniaxial compression.

Table 3. Comparison of data obtained from laboratory tests and numerical simulations

Parameter	Experiment	Numeric	Standard Deviation (%)
σ_{cm} (MPa)	22.97	23.06	0.39
E (GPa)	3.78	3.78	0.00
ν	0.17	0.17	0.00
σ_t (MPa)	3.24	3.22	0.62

and fjm_pb_fa were the σ_t, cohesion, and friction coefficient (tan ϕ_j) of the FJ bands, respectively, and the ratio of k_n to k_s of the FJ band was $\bar{k}_n/\bar{k}_s$.

To validate the accuracy of the resulting microparameters of the FJ–BPM, a number of two-dimensional (2D) numerical uniaxial compressive tests were simulated on 300×300 mm^2 dimensions and compared with the uniaxial compressive test result that was obtained from the laboratory experiment on an intact sample. Fig. 5 shows the simulation failure pattern with that of the experiments, which confirmed the validity of the estimated microparameters for further numerical simulations.

In addition, Fig. 6 shows a good agreement between the stress–strain curves of the uniaxial compression test and calibrated numerical model.

A number of Brazilian tests were performed on 54 mm diameter disks according to the ISRM suggested method (Bieniawski and Hawkes 1978). Their results were compared with the numerical simulation that led to a suitable agreement between the model simulation and the experimental data, as listed in Table 3.

SJ Calibration

The mechanical behavior of joints was controlled by the SJ parameters (Itasca Consulting Group 2022), which needed to be calibrated before modeling. The normal deformability (Bandis et al. 1983) [Fig. 7(a)] and direct shearing [Fig. 7(b)] were simulated

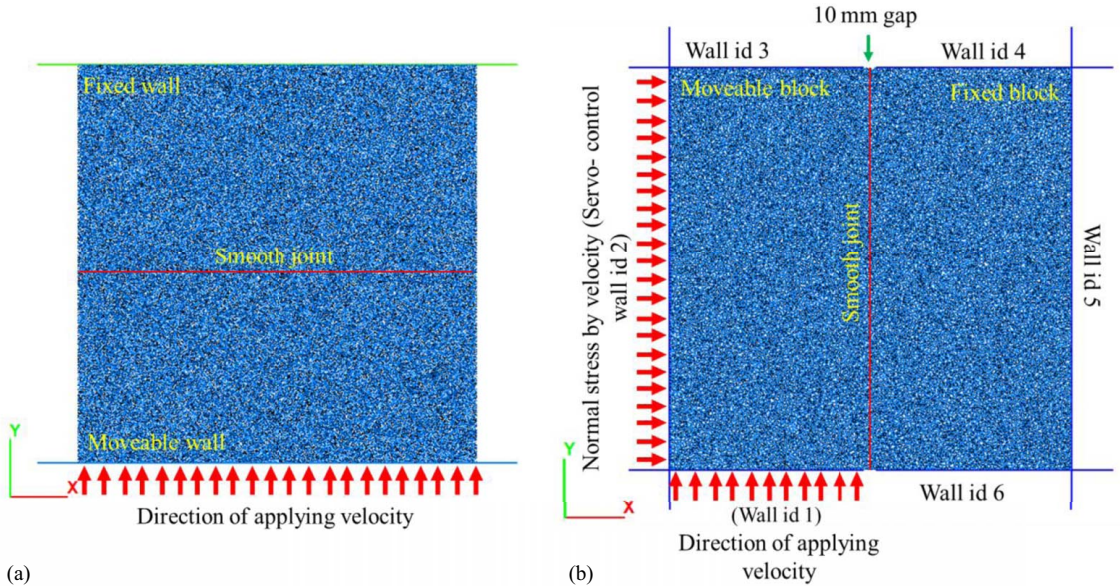

Fig. 7. SJ calibration from (a) normal deformability; and (b) direct shear modeling.

Table 4. Calibrated SJ parameters

SJ parameters	Value
k_n (GPa/m)	130
k_s (GPa/m)	1.50
tan tan ϕ_j	1.40

Table 5. Joint parameters obtained from the experiments and the numerical modeling

Joint parameter	Experiment	Numeric
Friction angle (°)	54.15	54.46
System k_s (GPa/m)	1.20	1.20
System k_n (GPa/m)	4.51	4.50

on 300×300 mm^2 samples where the planar joint was included to obtain the SJ parameters. These parameters were calibrated by trial and error to achieve the highest match with the macroscale properties that resulted from the laboratory experiment.

The same approach was deployed for the calibration of k_n. The SJ k_s and friction angle were calibrated against the laboratory data that were obtained from the direct shear test on the jointed sample with the planar joint. The SJ dilation angle value was set to that utilized by Bahaaddini et al. (2013b). The final calibrated parameters are given in Table 4.

A comparison between the resulting joint parameters from the laboratory test and the numerical simulation is presented in Table 5, which indicated a strong agreement between the experimental results and numerical data.

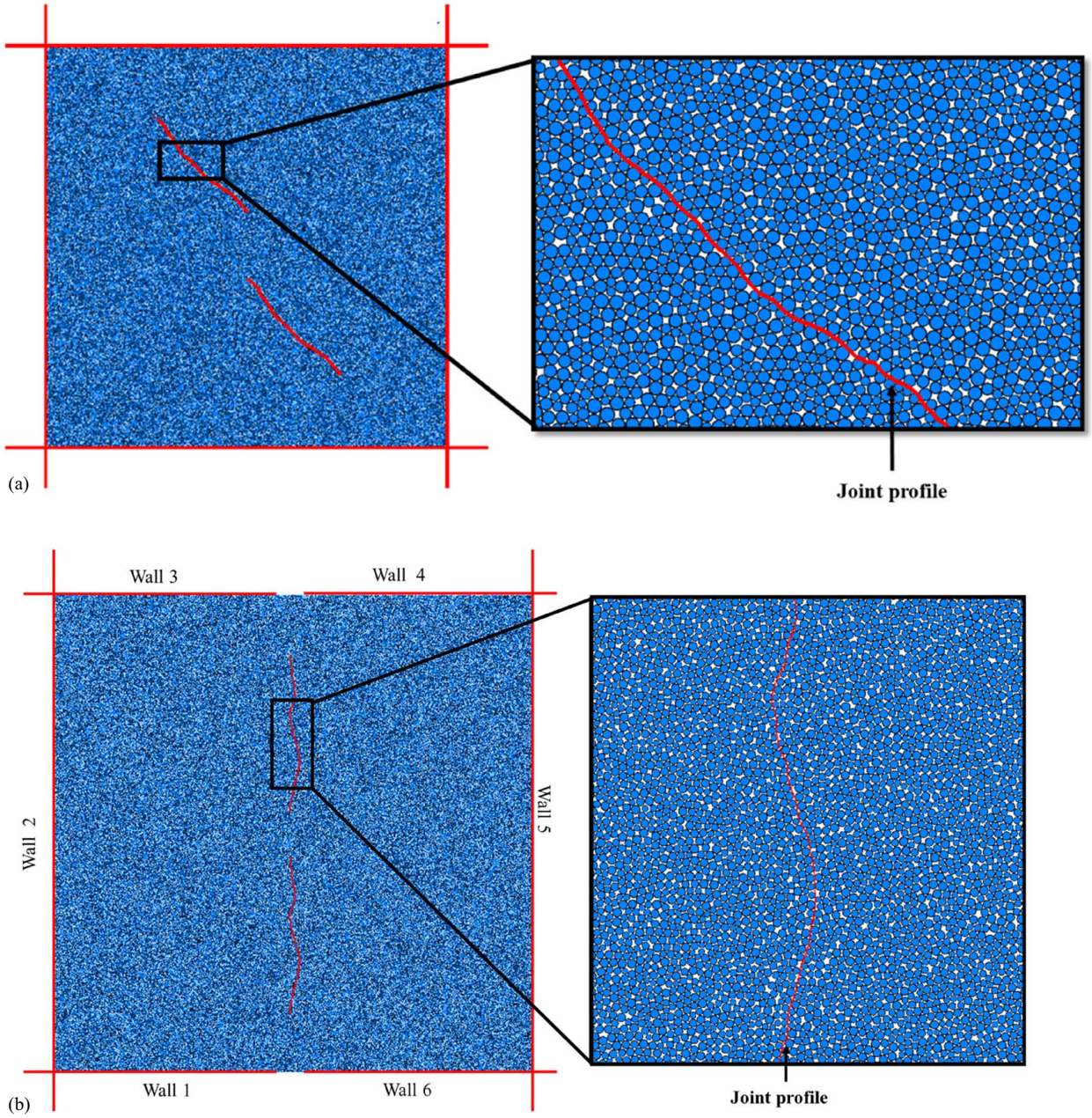

Fig. 8. Numerical model of a jointed rock sample with nonpersistent rough joints under (a) uniaxial compression; and (b) shearing.

Table 6. Comparison between the numerical and experimental results obtained from jointed rock samples under uniaxial compression

Sample number	JRC (level)	θ (°)	L (mm)	γ (°)	Experimental		Numerical	
					σ_{cm} (MPa)	E_{cm} (GPa)	σ_{cm} (MPa)	E_{cm} (GPa)
U1	10–12	0.0	25.0	135.0	21.66	4.44	22.33	4.36
U2	0–2	45.0	25.0	135.0	15.00	3.12	14.04	3.16
U5	18–20	45.0	25.0	135.0	19.03	3.53	19.24	3.47
U14	10–12	45.0	25.0	180.0	18.88	3.52	17.84	3.41
U19	10–12	90.0	25.0	135.0	17.60	3.54	22.46	3.74
U20	10–12	45.0	25.0	90.0	13.90	3.10	13.36	3.08
U21	10–12	45.0	10.0	135.0	15.50	3.01	15.37	3.13
U29	10–12	45.0	40.0	135.0	18.52	3.60	18.15	3.71
U30	10–12	45.0	25.0	135.0	16.78	3.21	16.51	3.41

Table 7. Comparison of the numerical and experimental results obtained from jointed rock samples under shearing

Sample number	JRC (level)	γ (°)	L (mm)	σ_n (MPa)	Experimental [τ_n (MPa)]	Numerical [τ_n (MPa)]
S1	10–12	180	44	0.50	3.02	3.20
S2	18–20	180	10	3.00	8.61	8.51
S3	18–20	120	44	2.17	8.24	8.12
S4	10–12	150	60	3.00	6.00	6.30
S5	10–12	120	10	1.33	5.34	5.25
S6	04–06	090	10	0.50	2.07	1.75
S7	18–20	150	27	0.50	3.03	2.25
S8	04–06	150	44	1.33	3.21	3.50
S9	14–16	120	60	0.50	2.67	2.50
S10	18–20	090	60	1.33	4.20	4.5
S11	14–16	150	10	2.17	7.34	7.01
S12	14–16	090	44	3.00	6.88	6.42
S13	04–06	120	27	3.00	6.27	6.43
S14	14–16	180	27	1.33	5.00	5.2
S15	10–12	090	27	2.17	7.00	6.50
S16	04–06	180	60	2.17	6.00	5.70

Numerical Modeling under Uniaxial Compression and Direct Shearing

Since joints do not demonstrate any asperity variation within the third dimension, they could be numerically simulated as a plane strain problem. Therefore, a three-dimensional experimental jointed rock sample could be modeled through a 2D numerical technique (Bahaaddini et al. 2013a, 2014a, 2016b).

Models Geometry

Numerical jointed rock samples of 300×300 mm^2 were generated in PFC2D according to Asadizadeh et al. (2018b). For the uniaxial compressive and shear loadings, the samples consisted of approximately 65,182 particles. They included the dense packing of non-uniform and well-connected circular particles with low locked-in stresses and the FJ bonds at the ball contact points (Fig. 8). The maximum ball diameter in the numerical models was 1 mm to

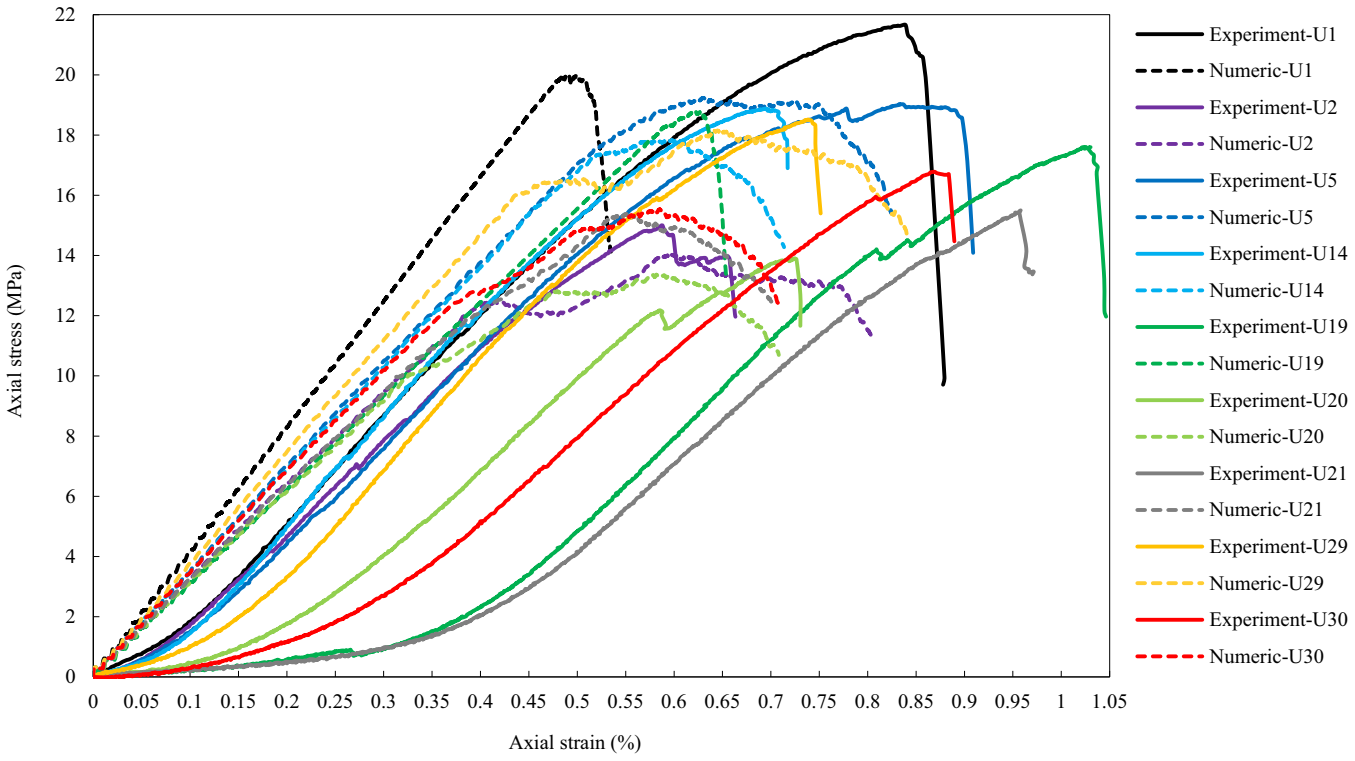

Fig. 9. Stress–strain curves obtained from all samples tested and simulated under uniaxial compressive loading.

generate the joint profiles. The joint roughness was created by summating the balls on the surface of the joint profile. The size of the balls should be small enough to generate the joint profile with an identical resolution to the physical models. Therefore, by trial and error and by considering the run time for the numerical models, a maximum ball diameter of 1 mm was the appropriate size to produce suitable results that agreed well with the physical models.

First, the frictionless joint profile was imported into the model; then, the sample vessel with the frictionless walls was filled with random circles. The particle sizes were controlled by the predefined minimum and maximum radii to satisfy a uniform particle size distribution. To reduce the magnitude of the locked-in stresses, isotropic loading was applied to the assembly of particles; then, those with <3 contacts were eliminated. In the next step, the joint walls were removed, and therefore, the FJ parallel bonds were installed between all particles that were in contact (Bahaaddini et al. 2013a; Potyondy and Cundall 2004). Finally, the SJ model was assigned to the location of the removed walls where the balls on both sides of the joint

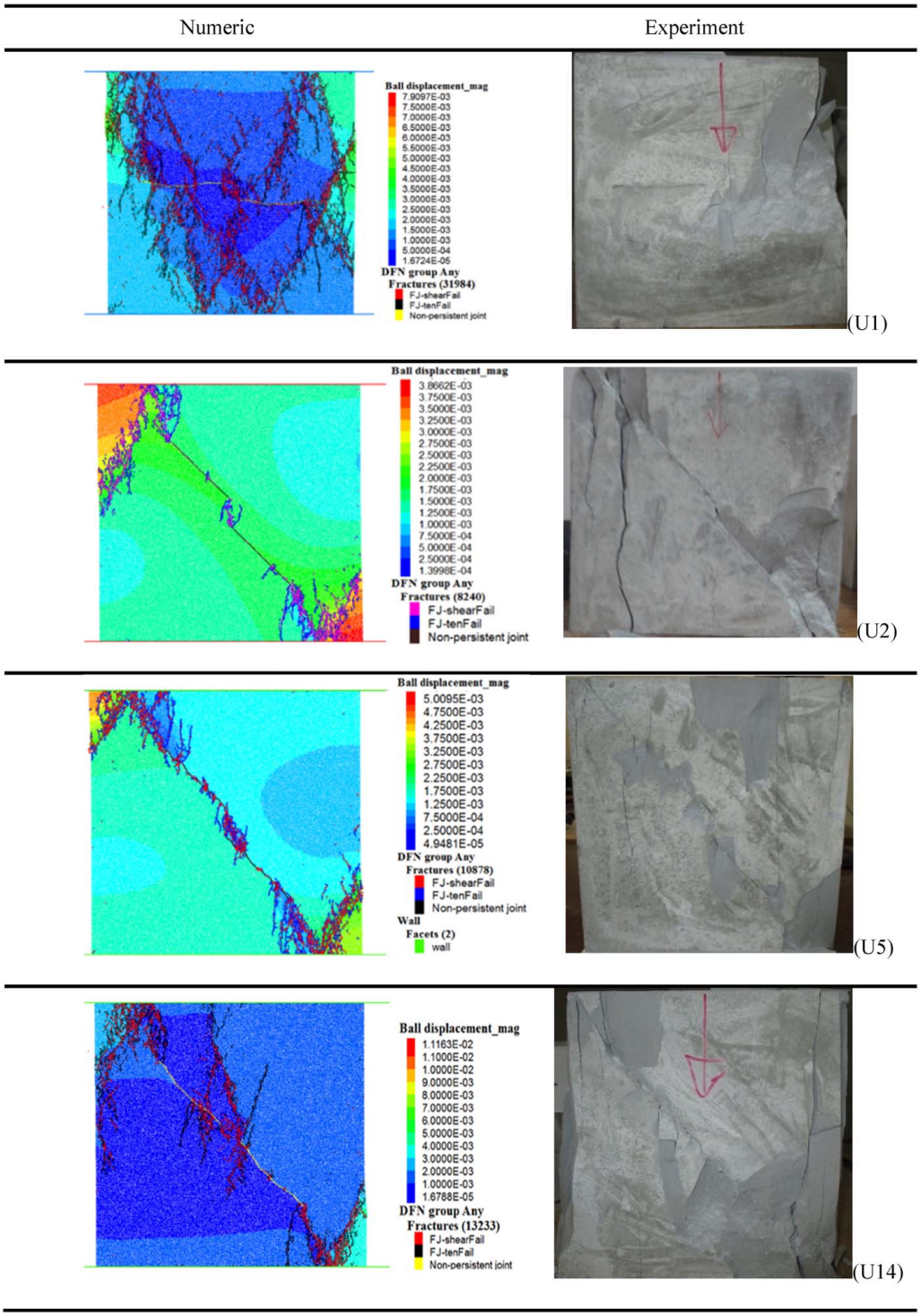

Fig. 10. Comparison of failure patterns in samples subjected to uniaxial compressive loading under a laboratory environment and numerical simulations.

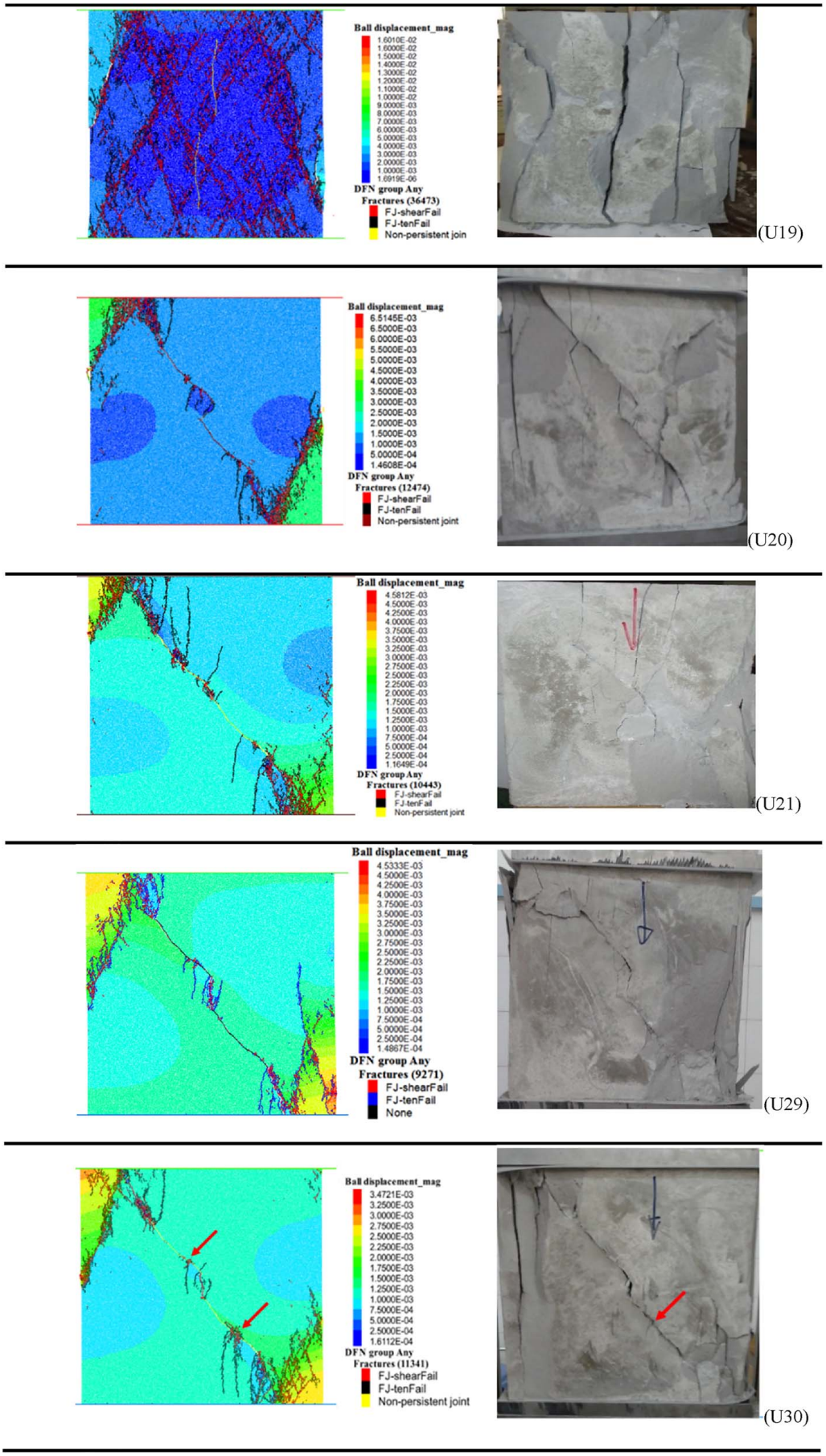

Fig. 10. *Continued.*

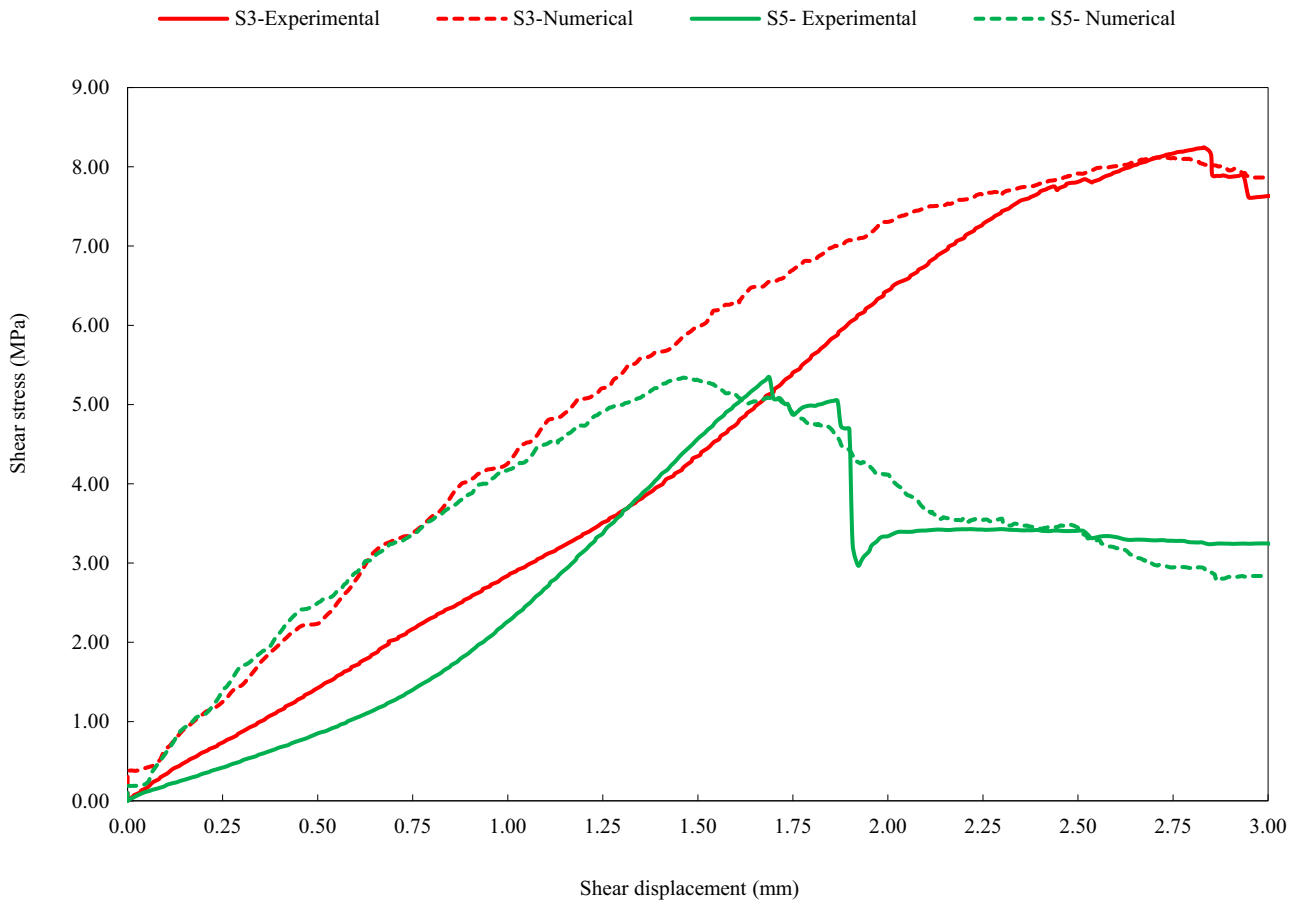

Fig. 11. Stress–displacement curves obtained from Samples S3 and S5 under experimental and numerical conditions.

were in contact with the SJ model. The number of SJs was used to define different roughness levels. For example, to achieve JRC = 4–6, 590 SJs were used, and for JRC = 10–12, 14–16, and 18–20, 594, 604, and 623 SJs were defined, respectively. Specifically, the numerical samples were loaded by pairs of opposing frictionless walls for the uniaxial compressive loading, as shown in Fig. 8(a). These walls were part of the material vessel commonly used to generate the FJ–BPM (Bahaaddini et al. 2013a).

The shear loading was under constant $\sigma_{n,}$ and the σ_n was applied horizontally to the left block (Wall 2). To accommodate a servo-controlled mechanism (Bahaaddini et al. 2015; Itasca Consulting Group 2022), σ_n remained constant during shear loading. The right block was restrained under the vertical and horizontal directions [Fig. 8(b)]. A vertical velocity of 5 μm/s was applied to Walls 1, 2, and 3. For the uniaxial compressive loading, the top and bottom sides acted as the loading platens, and they moved at a constant velocity rate of 5 μm/s, similar to that implemented by Asadizadeh et al. (2018b) for the laboratory uniaxial compressive tests on the artificial jointed rocks with nonpersistent rough joints.

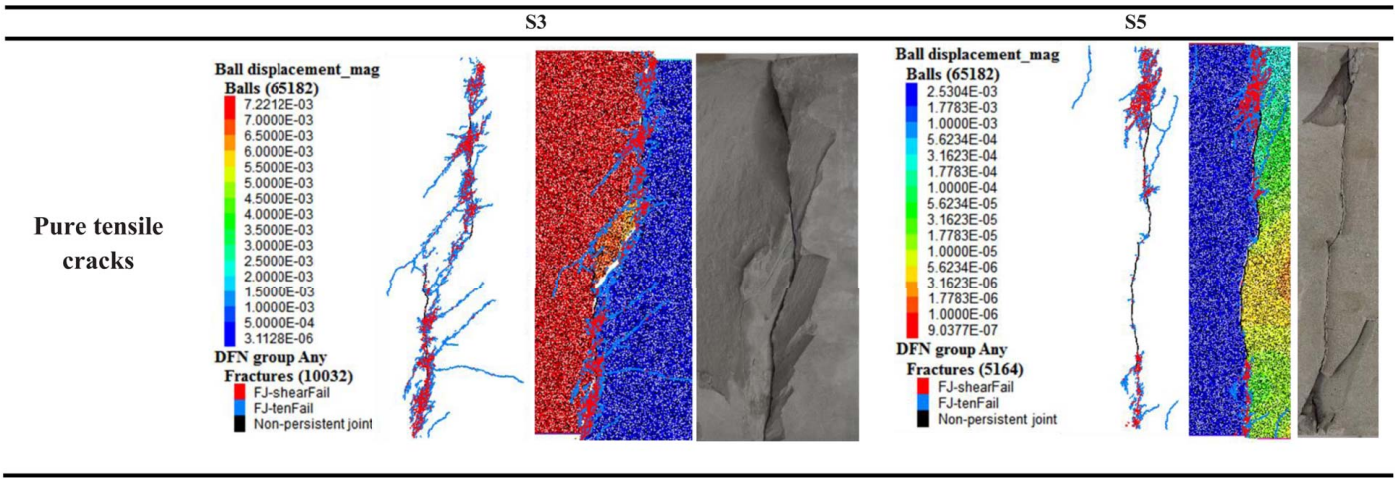

Fig. 12. Comparison of the tensile cracks obtained from numerical models and physical tests in Samples S3 and S5.

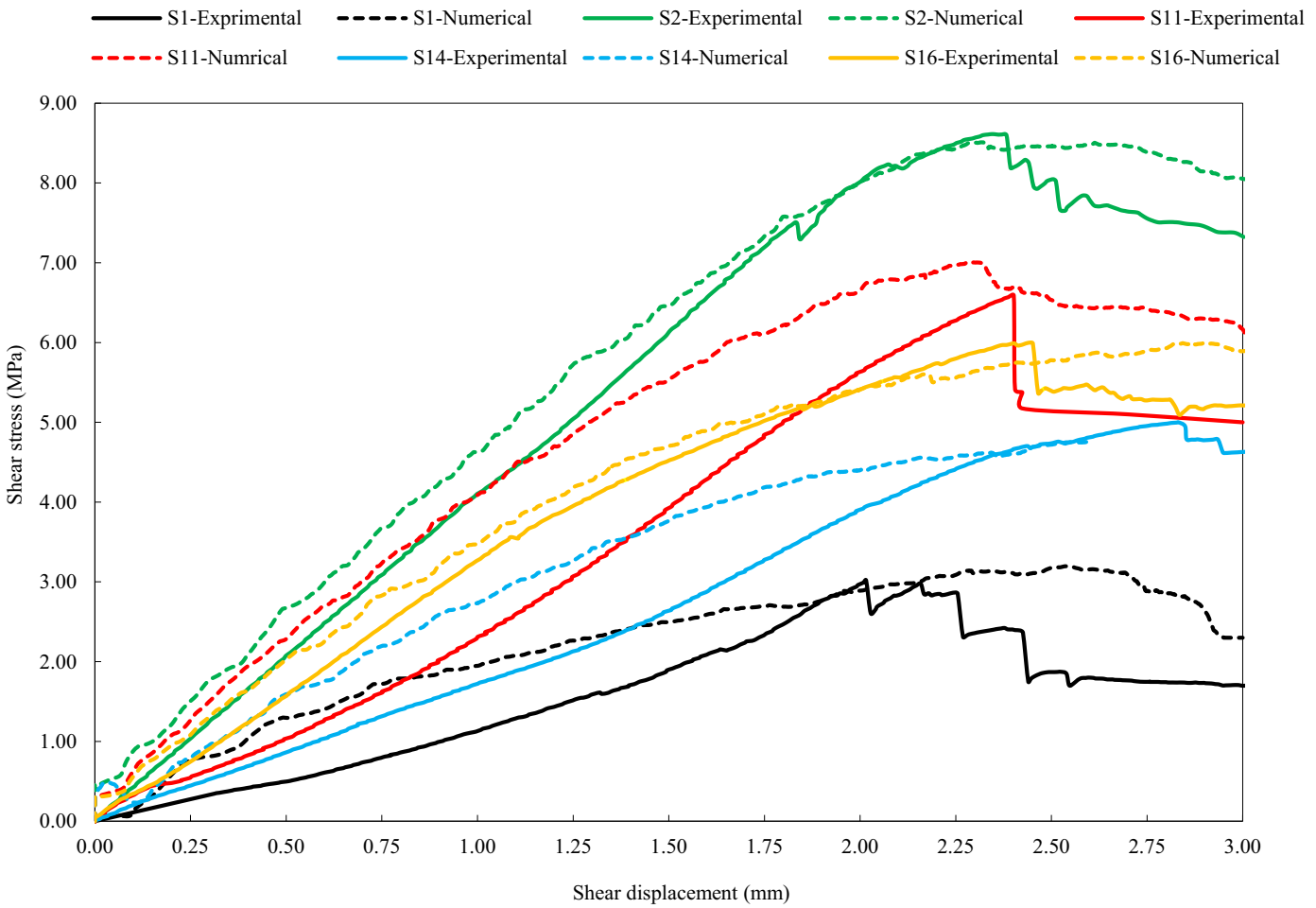

Fig. 13. Stress–displacement curves obtained from Samples S1, S2, S11, S14, and S16 under experimental and numerical conditions.

The time step (Δt) at each stage was $\Delta t \approx 3.722 \times 10^{-7}$s, which meant that the upper and lower sides moved vertically at 1.861×10^{-9} m/Δt. As confirmed in the preliminary study, this rate was low enough to ensure that the sample remained in a quasi-static condition. The left block could move vertically and dilate horizontally during shearing. The right block was fixed horizontally and vertically. The shear displacement was measured by recording the vertical displacement of Wall 1. The shear stress was measured by dividing the reaction force on Wall 4 over the shear plan length (which included the nonpersistent joint length).

Model Calibration and Validation

After the FJ–BPM and SJ parameters were calibrated, a large number of numerical models were generated to investigate the effects of γ, L, θ, JRC, and σ_n on the σ_{cm}, E_m, and τ_n of jointed rocks with nonpersistent rough joints under uniaxial compression and direct shearing numerically. Therefore, the 25 physical models reported by Asadizadeh et al. (2018b, 2019a), which included nine under uniaxial compression and 16 under shearing, were simulated for validation. Tables 6 and 7 give the results from the numerical modeling, which were in good agreement with the experimental data.

In the last step of model verification, the resulting failure patterns that were obtained from the laboratory experiments were compared with those from the numerical simulations, as presented in the following sections.

Simulation Validation under Uniaxial Compression

The resulting stress–strain curves that were obtained from the numerical modeling under uniaxial compression were compared with those reported by Asadizadeh et al. (2019a) from the laboratory experiments shown in Fig. 9. Fig. 10 shows the resulting failure patterns from the numerical simulations with those that were obtained from the laboratory tests. There was good agreement between the numerical and experimental data, particularly when the σ_{cm} and E_m values were compared. Of note, the initial nonlinearity at the start of loading that was observed from the laboratory results was associated with the engagement phase between the loading platens and the samples, as discussed by Korinets and Alehossein (2002). Such behavior is not observed often in numerical simulations.

In Sample U1 with $\theta = 0°$, the failure pattern (Fig. 10) on the right side of both samples was similar. On the left side of the numerical model, there were some shear cracks, which might be related to the bridge failure under numerical simulation, as shown in red. In Sample U30 with $\theta = 45°$, the failure modes from the numerical and experimental conditions were very similar. In addition, a set of interlocking cracks, which are shown by red arrows in Fig. 10, were visible in the numerical model, and they were not clear in the physical sample due to unloading after the experiment.

In Sample U2 with JRC = 0–2 (Fig. 10), the numerical simulation demonstrated the growth of wing cracks near the bridge area at the crack tips. After the creation of the shear surface, the growth of these cracks stopped; however, for the sample that was tested under

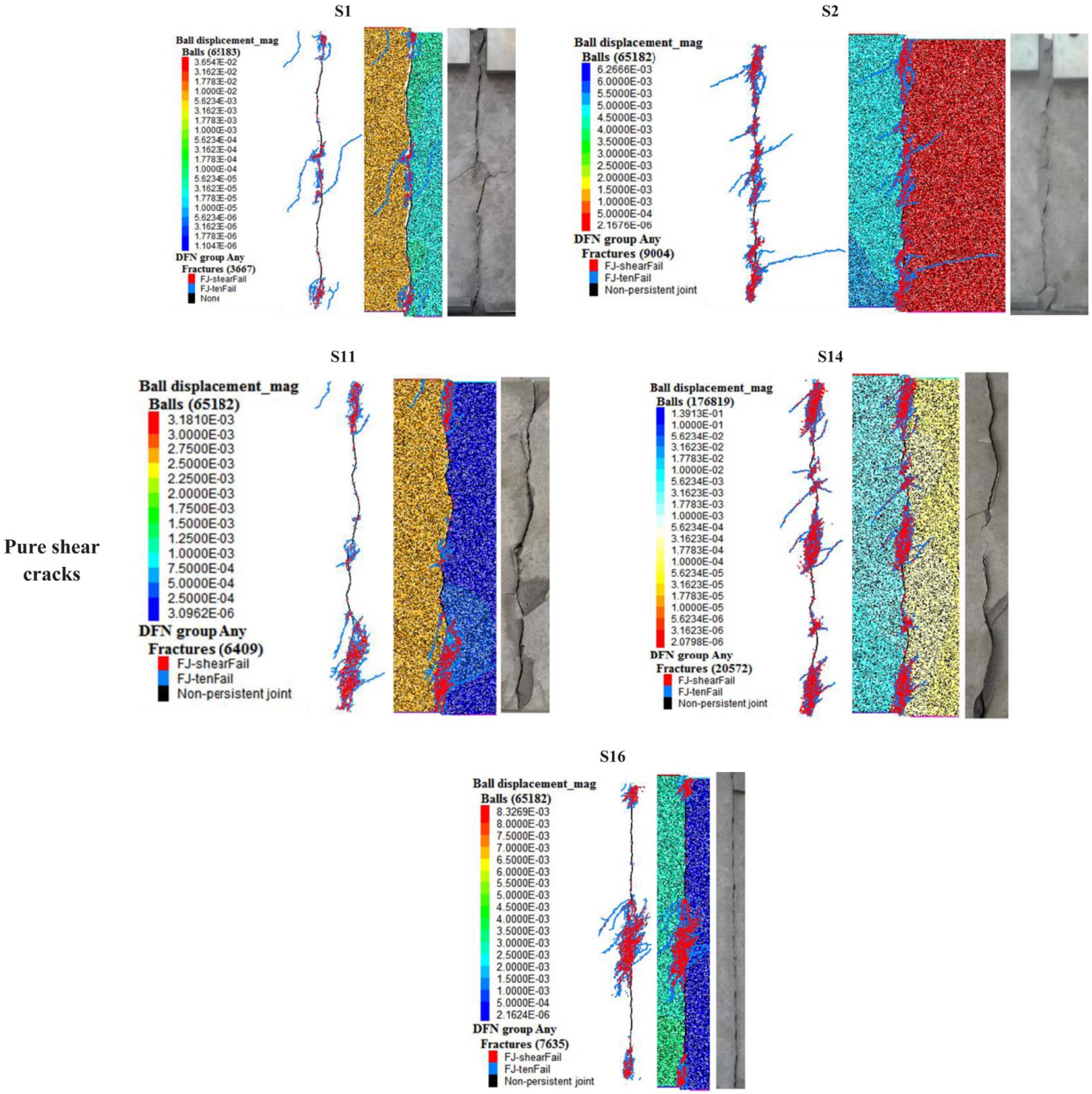

Fig. 14. Comparison of shear cracks obtained from numerical models and the physical tests in Samples S1, S2, S11, S14, and S16.

laboratory conditions, the propagated wing cracks were not visible due to unloading after the test. In both cases, crack coalescence occurred in the bridge area.

In Sample U20 with $\gamma = 90°C$, pure tensile failure was the dominant failure mode in the bridge area, as seen in the numerical and physical models. In contrast, in Sample U14 with $\gamma = 180°C$, the bridge area failed through shear cracking under numerical and experimental conditions. In the numerical model, in the bridge area, in addition to tensile cracks, two shear surfaces coincided in an inverted Y-shape, possibly due to stress concentration at the crack tips and joint asperities.

In Sample U21 with $L = 10$ mm, shear failure was the dominant failure mechanism in the numerical and experimental models, which is known as interlocking cracks and demonstrated the validity of the numerical results. In Sample U29, with the longest L, tensile and shear failures contributed to the bridge failure, which was visible from the numerical model and physical test.

Simulation Validation under Direct Shear Testing

Asadizadeh et al. (2018b) grouped the resulting laboratory failure modes from direct shear tests into three main categories: (1) tensile; (2) shear; and (3) a mixed mode of tensile and shear cracking. The numerical and experimental data were compared based on the three

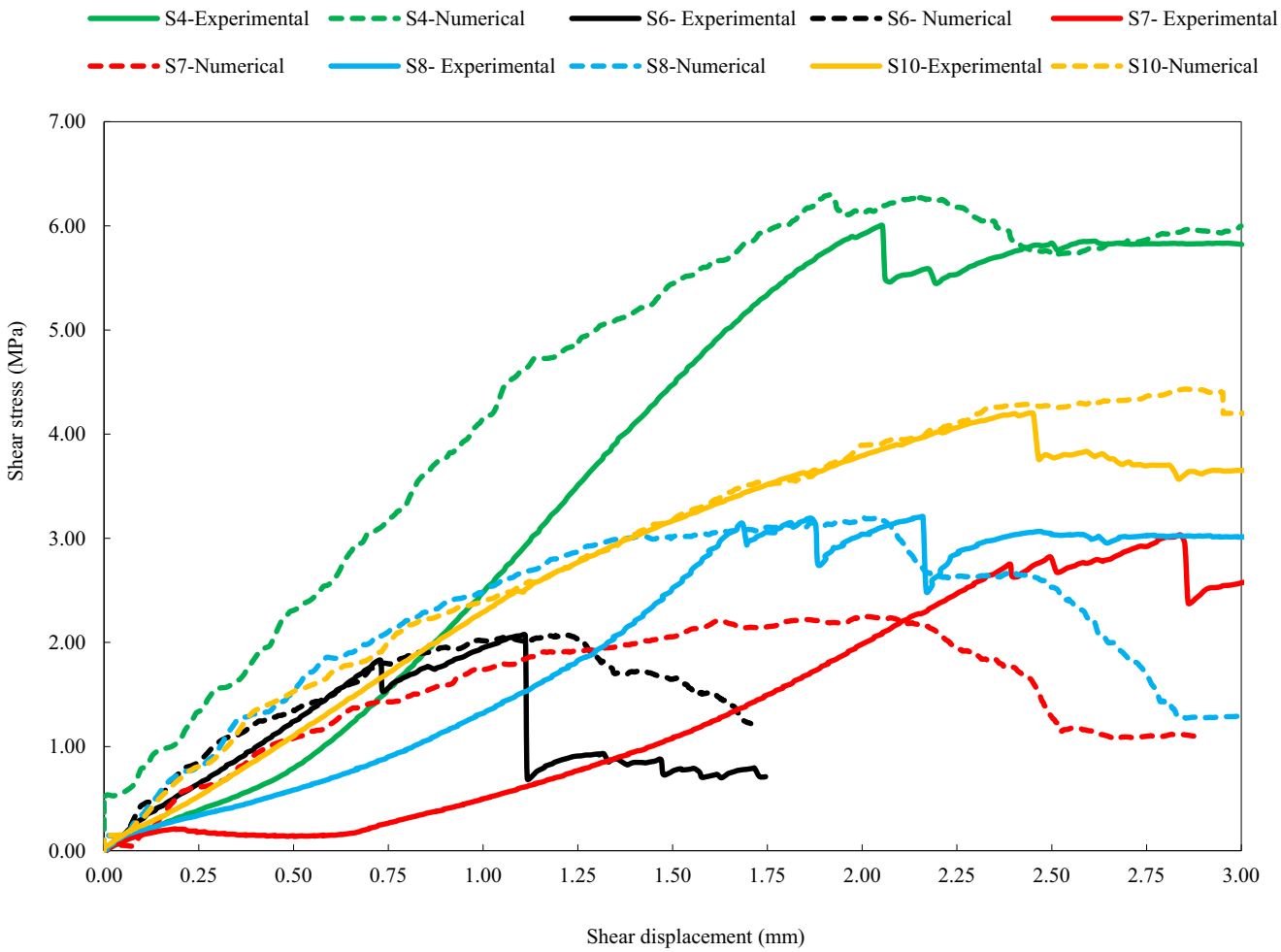

Fig. 15. Stress–displacement curves obtained from Samples S4, S6, S7, S8, and S10 under experimental and numerical conditions.

categories for verification, and the resulting stress–displacement data and failure patterns were examined.

Tensile Cracking Failure Mode

In this category, the tensile mode controlled the cracking within the bridge area. A comparison between the stress–displacement curves that resulted from the experimental and numerical simulations is shown in Fig. 11, which exhibits a reasonable agreement between both data sets. The slight distinction between the curvatures of both scenarios could be associated with the limitations within the laboratory environment and boundary conditions during the experiments.

The numerical and experimental failure patterns of Samples S3 and S5 are shown in Fig. 12. Both samples showed tensile failure within the bridge zone, which was highlighted in blue for numerical models where the FJ bonds failed. Of note, the formed cracks were classified based on their formation status, which included flat-joint bond failure in shear (FJ–shearFail), which is shown in red. Those that failed in tension (FJ–ten Fail) are in blue, and the remaining SJ contacts (nonpersistent rough joints) are in black. In addition, to better understand the failure details under numerical modeling, the total displacement field of both samples under direct shearing (Ball displacement_mag) is shown in Fig. 12. The failure modes from the numerical modeling matched well with the experimental data.

Shear Cracking Failure Mode

Samples S1, S2, S11, S14, and S16 experienced failure in shear in the laboratory environment, as reported by Asadizadeh et al. (2018b). The stress–displacement curves of these samples are shown in Fig. 13, where the numerical and experimental results were compared, which led to a reasonable agreement in all cases.

The failure patterns that were obtained from the numerical simulations and physical tests in Samples S1, S2, S11, S14, and S16 are shown in Fig. 14, where the cracking primarily happened in the bridge area (red cracks in the numerical models). Both physical and numerical scenarios exhibited some crushed materials inside the cracks at the end of the loading (red cracks on the joint surfaces in the numerical models). In this category, under numerical modeling, the tensile cracks in the bridge zone (blue) did not contribute to the cracking. In Samples S2 and S14, due to a high JRC and σ_n, the interlocking cracks were the main failure mode, and for the other samples, this mechanism was not observed.

Mixed Mode of Tensile and Shear Cracking

This category was divided into two subcategories by Asadizadeh et al. (2018b), which included the failure modes with only tensile and shear cracks and the mixed mode of tensile and shear cracks with additional tensile–shear cracks or both. Samples

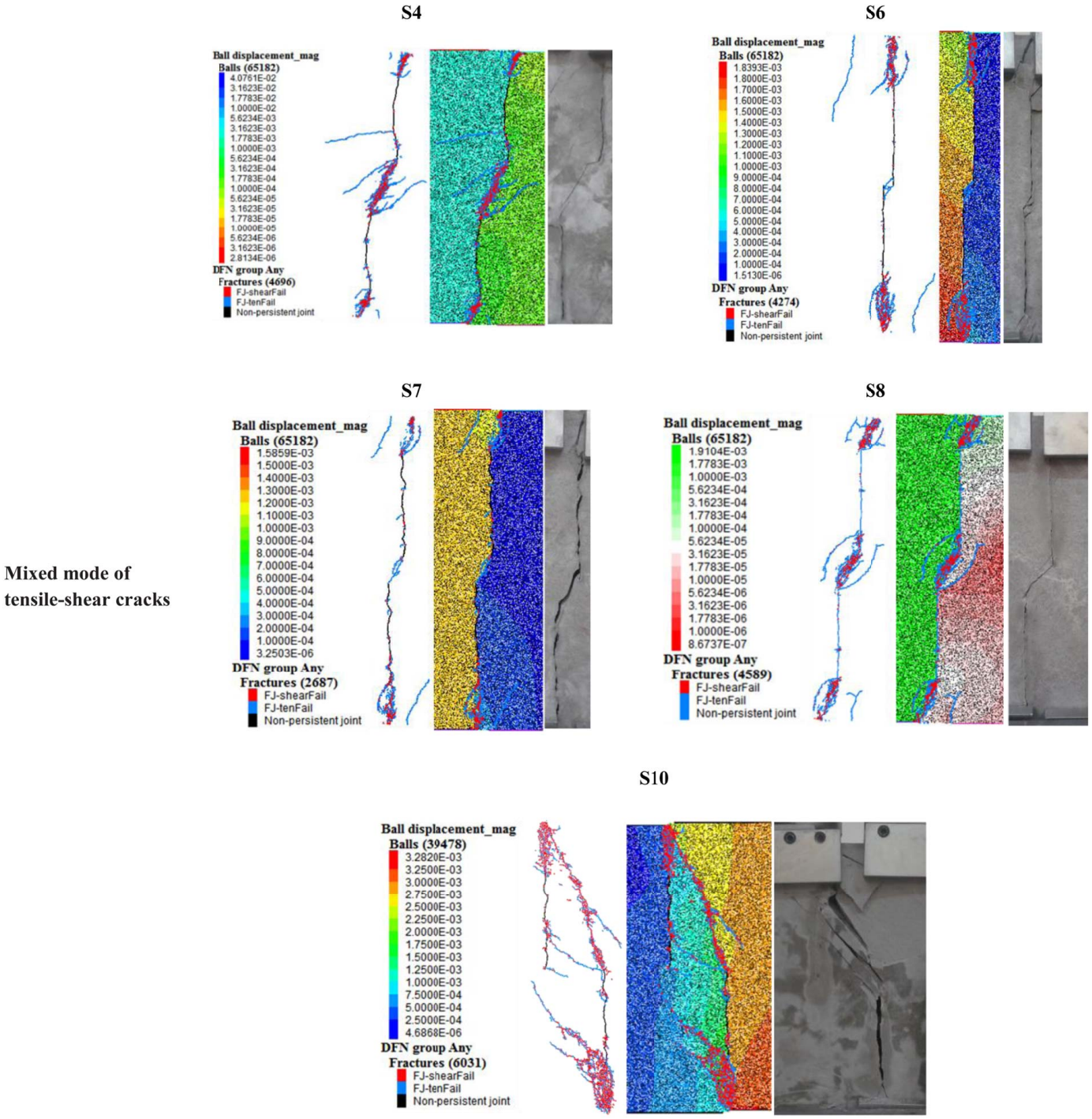

Fig. 16. Comparison of the mixed mode of tensile–shear cracks obtained from numerical models and physical tests in Samples S4, S6, S7, S8, and S10.

S4, S6, S7, S8, and S10 were classified in the first subcategory, which failed under tensile and shear cracking. The resulting experimental and numerical shear stress–displacement curves of these samples are shown in Fig. 15, which indicated a suitable agreement between the laboratory data and the numerical results.

Fig. 16 shows the failure processes in the physical tests and the numerical models that were obtained from Samples S4, S6, S7, S8, and S10. An S-shaped mixed mode was the typical failure pattern that was reported for Samples S4, S7, and S10 from the laboratory tests, which was evident in the numerical models. From Fig. 16, it can be seen that the bridge breakage in Sample S6 under the numerical simulation was controlled by tensile cracks. Under laboratory conditions, the failure in the central part of the bridge zone was the key driver.

The shear stress–displacement curves that were obtained from the experimental and numerical results for the second subcategory samples (e.g., S9, S12, S13, and S15) are shown in Fig. 17. The differences between the numerical results and those from the experiments during the early loading stage in Samples S9, S13, and S15 might be related to the adjustment in loading at the start of the experiment. Such a limitation

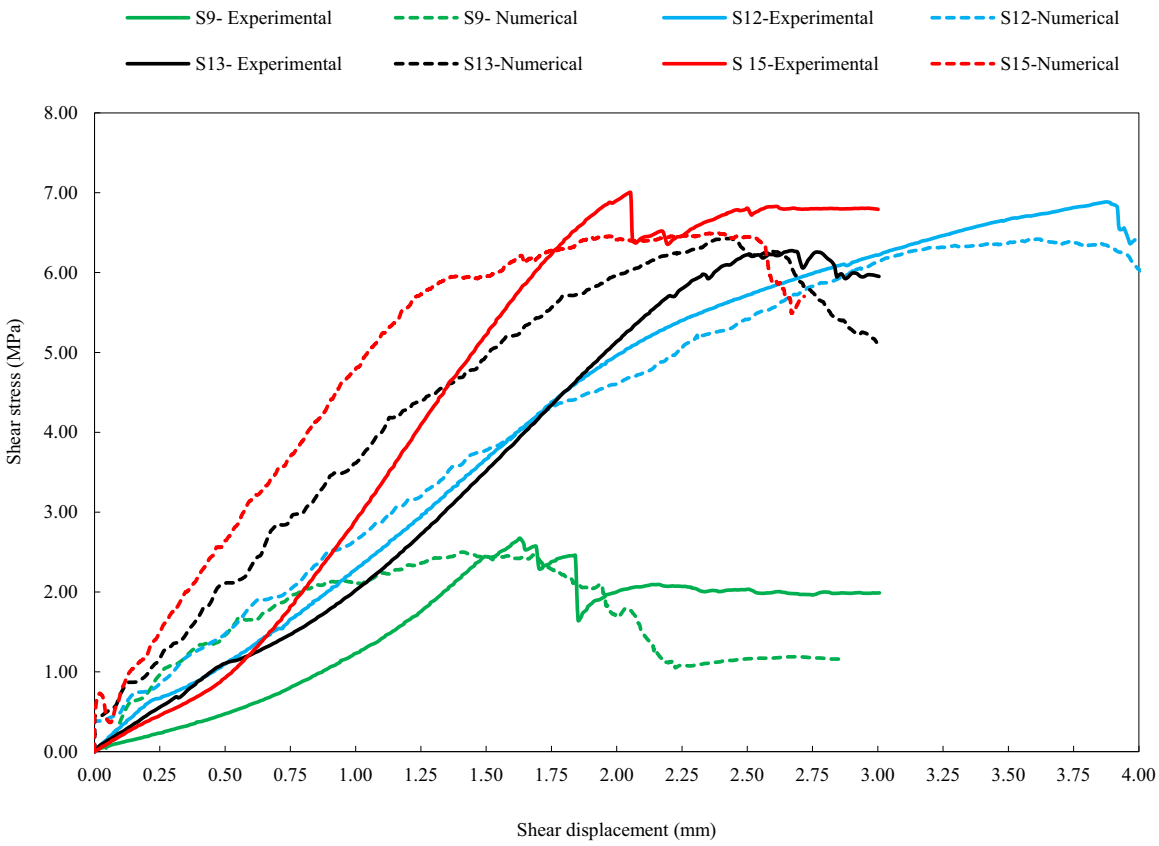

Fig. 17. Stress–displacement curves obtained from Samples S9, S12, S13, and S15 under experimental and numerical conditions.

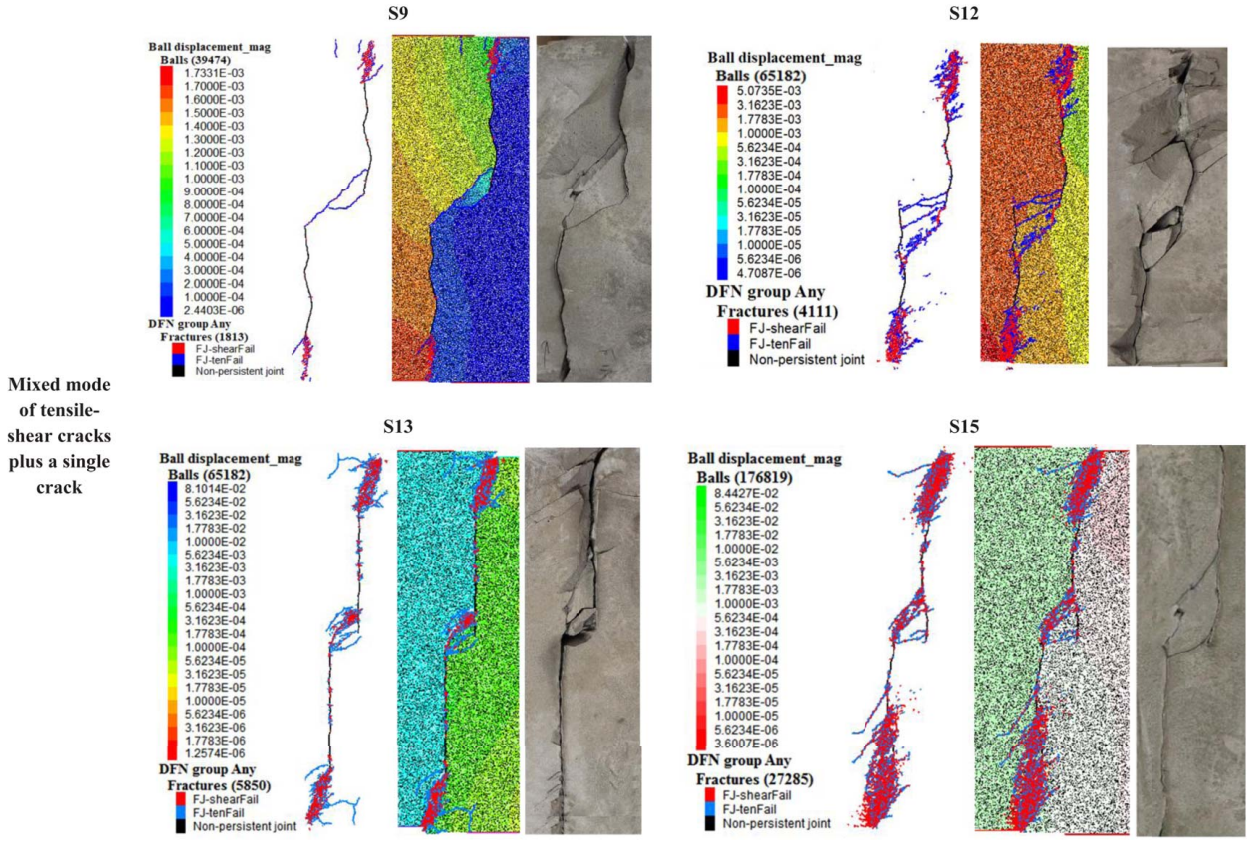

Fig. 18. Comparison of mixed mode of tensile–shear cracks plus a random shear or tensile crack obtained from numerical models and physical tests on Samples S9, S12, S13, and S15.

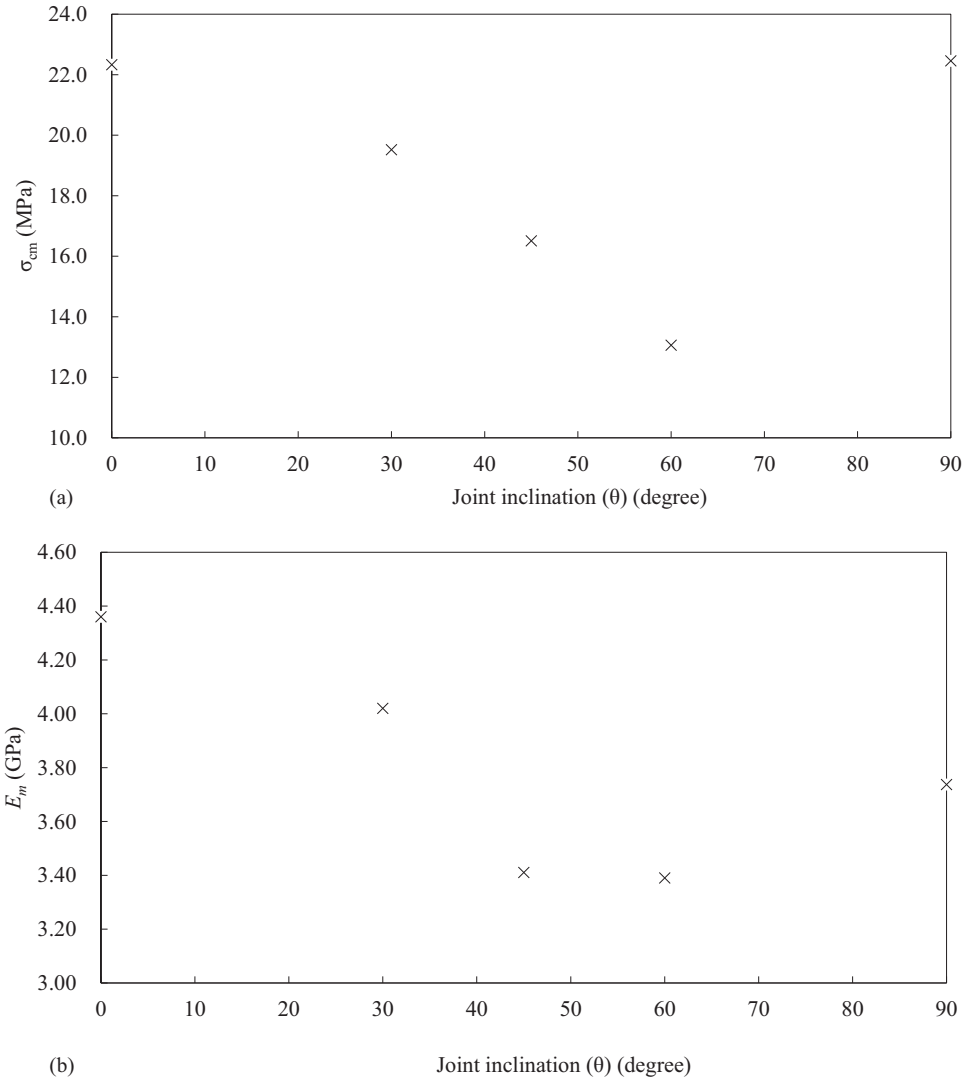

Fig. 19. Effect of θ on (a) σ_{cm}; and (b) E_m obtained numerically from the uniaxial loading on nonpersistent jointed rock.

could have been avoided during numerical modeling, which led to some variations between the laboratory data and the numerical results.

Fig. 18 shows the failure processes in Samples S9, S12, S13, and S15 that were obtained from the physical tests and the numerical modeling, which exhibited a mixed mode of tensile and shear cracking plus a single random tensile or shear crack. Asadizadeh et al. (2018b) argued that the high σ_n or JRC could trigger the interlocking of asperities that led to the formation of tensile cracks from the asperities toward the boundary of the sample, which are shown in Fig. 18 for the physical tests and numerical simulations.

Parametric Study

An extensive parametric study on the effects of γ, L, θ, JRC, and σ_n on σ_{cm}, E_m, and τ_n of jointed rock was conducted numerically to expand on the works by Asadizadeh et al. (2018b 2019a) within a laboratory environment under uniaxial compression and direct shearing. Some additional scenarios were simulated; therefore, the role of each parameter under uniaxial compressive and shear loadings could be explored further.

Numerical Models under Uniaxial Compressive Loading

Effect of θ under Uniaxial Compression

Five different levels were considered for θ that included 0°, 30°, 45°, 60°, and 90° and the rest of the parameters remained constant at their mean level (e.g., $L = 35$ mm, JRC = 10–12, and $\gamma = 135°$). Fig. 19 shows the σ_{cm} and E_m that were obtained from the numerical models at various θ. For σ_{cm} and $E_{m,}$ there was a descending and then ascending trend in which both parameters reduced with an increase in θ from 0° to 60° and then they increased to 90°. The σ_{cm} reached its minimum at $\theta = 60°$, and for $E_{m,}$ this potentially happened between 45° and 60°. In the samples with θ<30°C, the increase in σ_{cm} was due to the reduction in the stress concentration at the joint tips, which could then lead to a uniform distribution of stress across the bridge areas that resulted in a higher σ_{cm}. Given that E_m was a function of σ_{cm}, the same argument could be applied.

Effect of JRC under Uniaxial Compression

The impact of JRC on σ_{cm} and E_m under uniaxial loading was explored numerically, and the results are shown in Fig. 20. With an increase in JRC, σ_{cm} and E_m increased, which confirmed the role

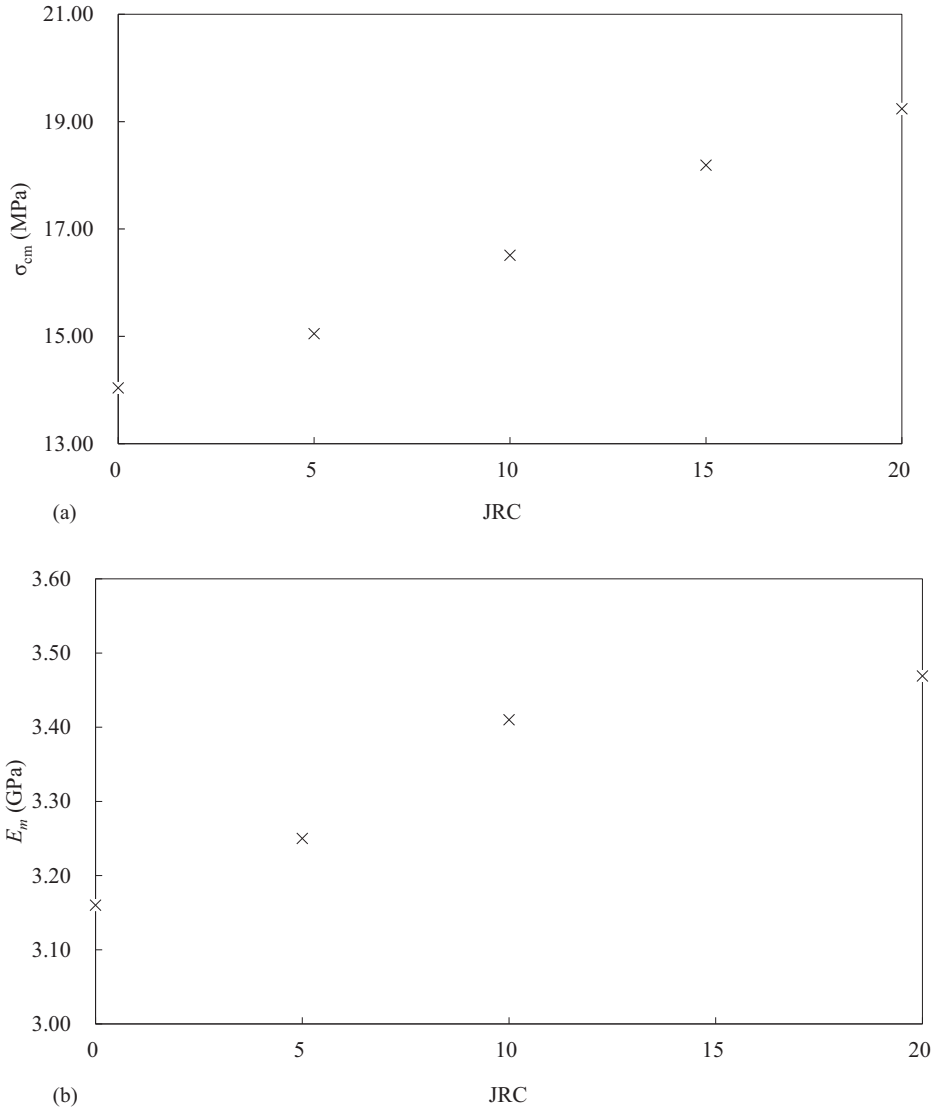

Fig. 20. Effect of JRC on (a) σ_{cm}; and (b) E_m obtained numerically from the uniaxial loading on nonpersistent jointed rock.

of high roughness when interlocking cracks were created during the failure of samples under axial loading and led to higher σ_{cm} and a greater E_m.

Effect of γ under Uniaxial Compression

As with the JRC, with an increase in γ, σ_{cm}, and E_m increased, in particular, between 115°C and 155°C as shown in Fig. 21. These behaviors could be associated with the transition in the failure mode of the bridge area from pure tensile failure to pure shearing, as discussed previously for the physical tests in shown Fig. 10. The reduction in E_m at 180°C might be explained by the development of interlocking cracks from joint asperities [i.e., Sample U14 (Fig. 10)].

Effect of L under Uniaxial Compression

The effect of L on σ_{cm} and E_m was investigated numerically, and the results are shown in Fig. 22. There was an increasing trend in σ_{cm} with an increase in L from 10 to 50 mm. As L increased, the bearing capacity of the bridge area increased, which led to higher σ_{cm} and E_m at larger L.

Numerical Models under Shear Loading

Effect of γ under Shearing

The γ varied from 90° and 180° in 30° increments, and the remaining parameters remained constant at their medium values (e.g., $L =$ 35 mm, JRC = 10–12, and $\sigma_n = 1.75$ MPa). The effect of γ on τ_n is shown in Fig. 23, followed by the crack coalescence patterns in the bridge areas of the simulated samples in Fig. 24. The trend of τ_n verses γ fluctuated where it increased from 90° to 120° and then decreased to 150° and again increased at 180°. From Fig. 24, it can be seen that an increase in γ led to the formation of wing cracks followed by the shearing process. The reduction in τ_n at 150° might be associated with the initiation and propagation of wing cracks in the bridge area, which agreed with Asadizadeh et al. (2018b), who proposed the formation of interlocking cracks as a key factor when reducing τ_n.

Effect of L under Shearing

The τ_n that were simulated with various L are shown in Fig. 25. From this figure, τ_n had an approximately linear reverse correlation

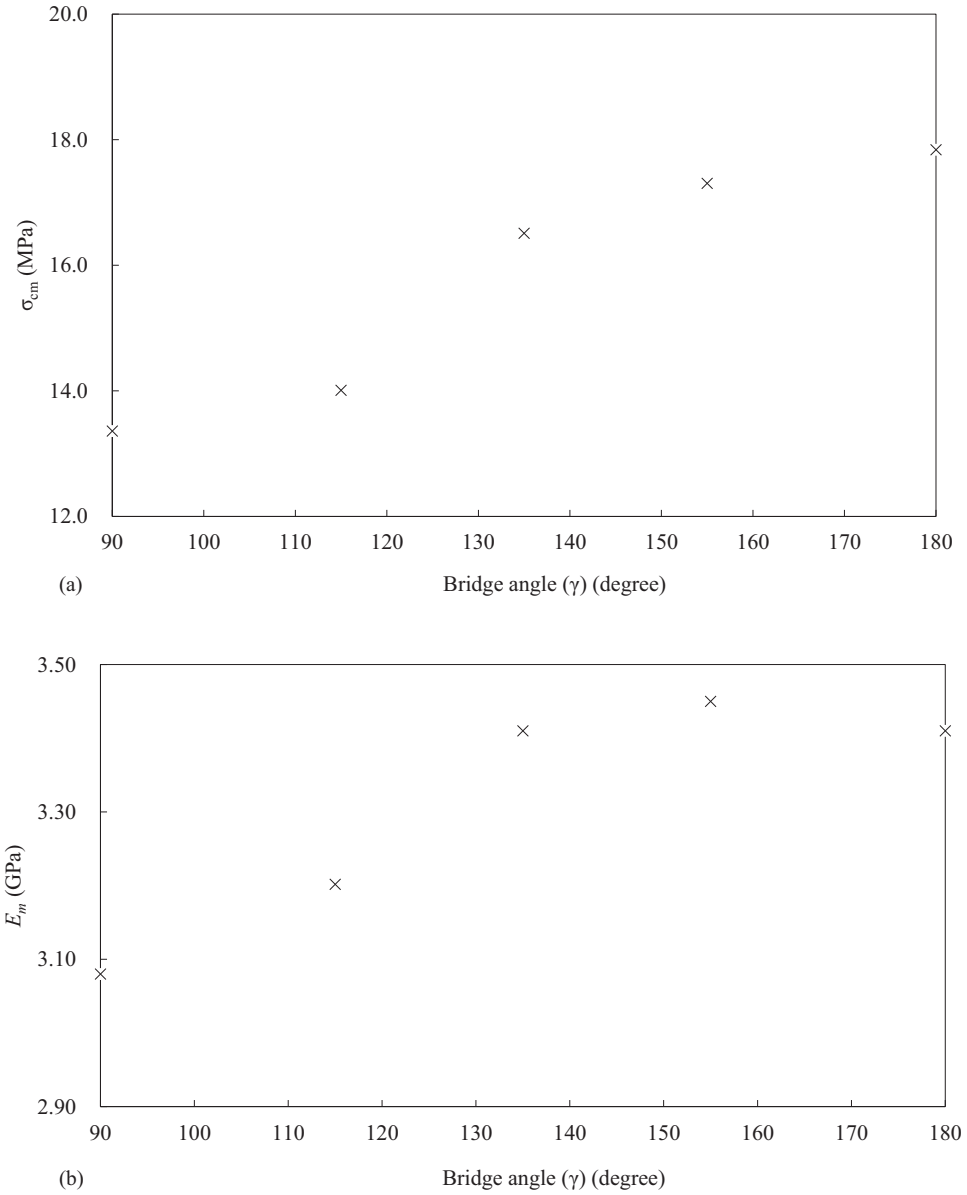

Fig. 21. Effect of γ on (a) σ_{cm}; and (b) E_m obtained numerically from the uniaxial loading on nonpersistent jointed rock.

with L. The governing mechanism in the reduction of τ_n was the decrease in the distance between the outer tip of the cracks and the model boundary, because of an increase in the central L (green dash line in Fig. 26). In the bridge area, with an increase in L from 10 to 60 mm, the wing cracks formed and after the development of tensile cracks, at a larger L, the shear cracks added to the wing cracks. This was similar to the samples with $L = 40$ and 60 mm, which led to the reduction in τ_n. With an increase in the length of the central bridge (where the tensile mode was dominant), the outer ligament length decreased (where the shear mode was controlling), which resulted in sample failure at lower τ_n. Therefore, a decrease in the shear surface led to an increase in the area under tensile failure mode and then sample failure at lower τ_n. The numerical simulations showed that the variation in L, which was mutually intertwined with the dimension of the outer ligaments, could easily change the length of the shear surface in the bridge area. In addition, in all the numerical samples with different L, tensile cracking was the dominant process in the bridge area.

Effect of JRC under Shearing

To investigate the effect of JRC on τ_n in jointed rock samples numerically, four different ranges of JRC were considered, which included 4–6, 10–12, 14–16, and 18–20. From the numerical simulations, an increase in the JRC could lead to an increase in τ_n (Fig. 27), which agreed with Asadizadeh et al. (2018b) from a limited number of laboratory experiments. The cracking processes in the simulated samples with various JRC are shown in Fig. 28, where the wing cracks developed in the bridge area, followed by shear failure in the sample with JRC = 4–6. With an increase in JRC, the τ_n increased, which could be associated with the effect of joint asperities. In addition, at a high level of JRC, interlocking cracks could be initiated and propagated, which might lead to an increase in τ_n.

Effect of σ_n under Shearing

To further investigate the effect of σ_n on τ_n, σ_n was varied between 0.5 and 3 MPa, and the rest of the parameters were at their middle

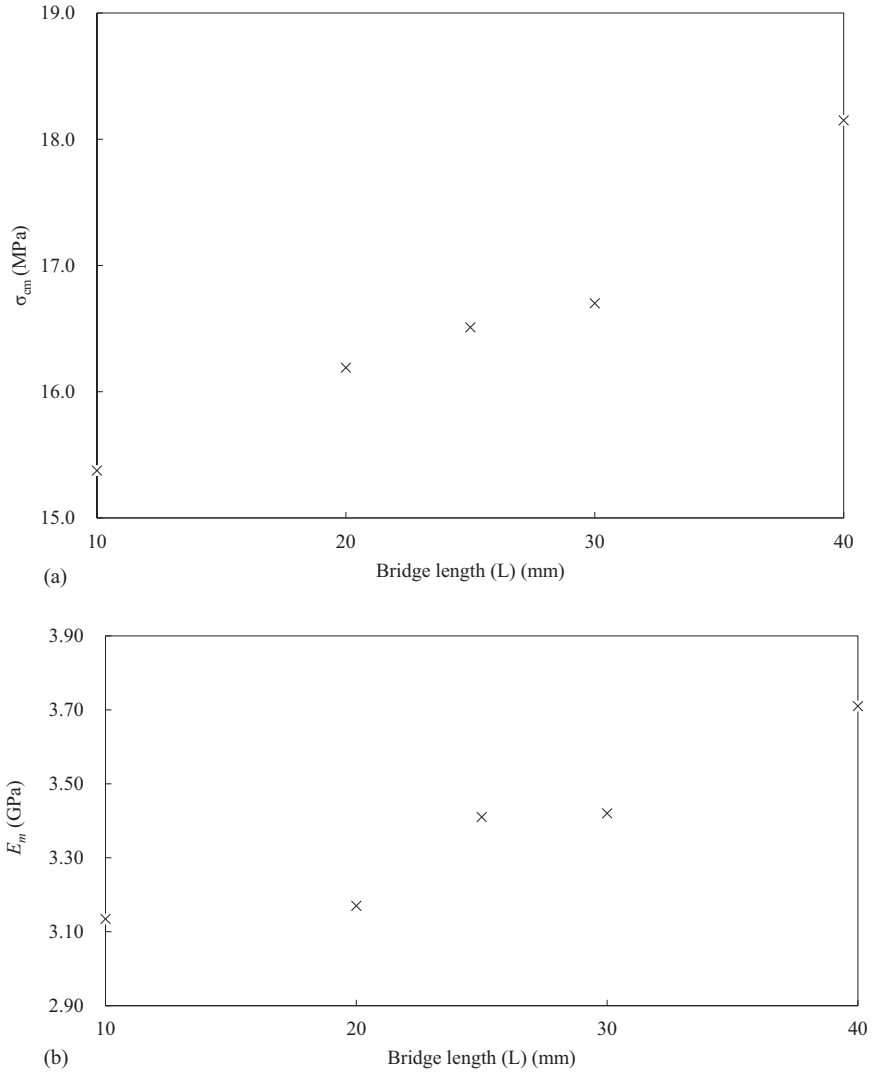

Fig. 22. Effect of L on (a) σ_{cm}; and (b) E_m obtained numerically from the uniaxial loading on nonpersistent jointed rock.

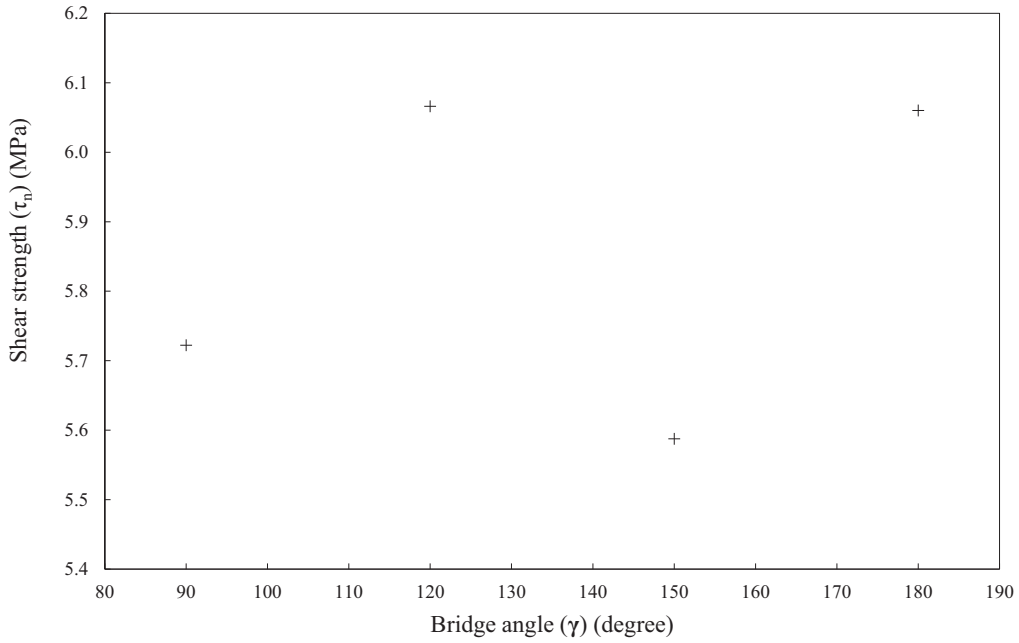

Fig. 23. Effect of γ on τ_n obtained numerically from the shear loading on nonpersistent jointed rock.

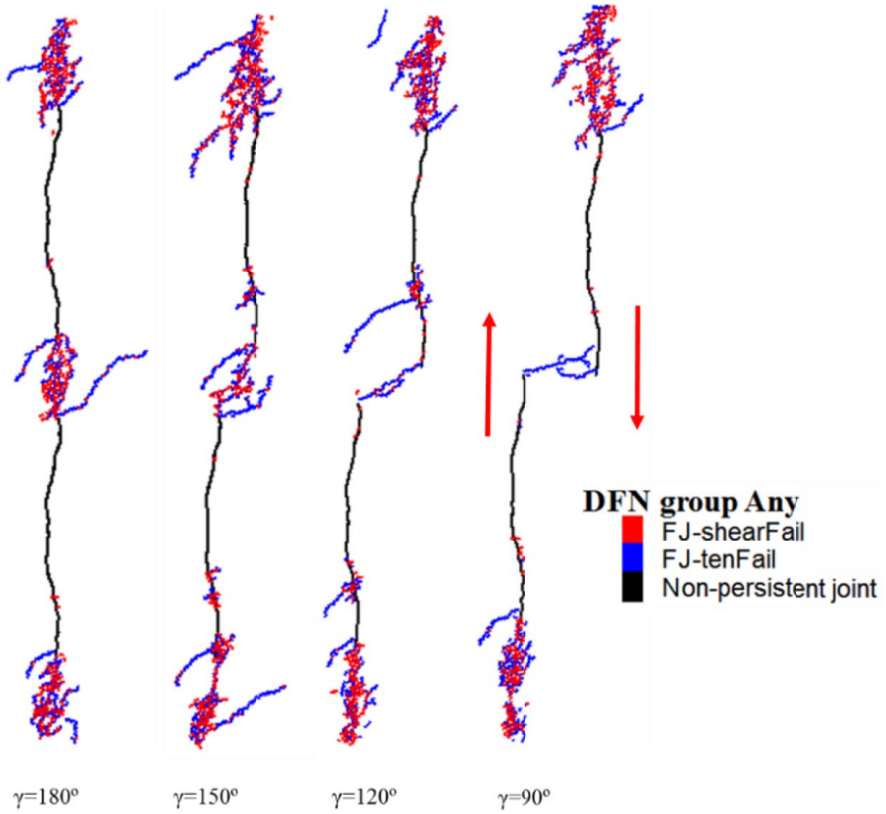

Fig. 24. Numerical simulations of cracking processes at different γ under shearing.

values, which was similar to previous parametric analyses. The impact of σ_n on τ_n and the cracking processes are shown in Figs. 29 and 30, respectively. There was a direct correlation between τ_n and σ_n where an increase in σ_n led to an increase in τ_n approximately linearly (Fig. 29).

The cracking processes that were due to changes in σ_n indicated that in the bridge area, the wing cracks developed first, followed by the mixed mode of cracking. This behavior was observed in the sample that was simulated under $\sigma_n = 3$ MPa. Therefore, with an increase in σ_n, the initiation and propagation of interlocking cracks might become evident. This cracking process could reduce the stiffness and then the sample's integrity. Under a high σ_n, the shear mode dominated the cracking process at the outer tips of the joints. Therefore, more crushed materials were produced inside

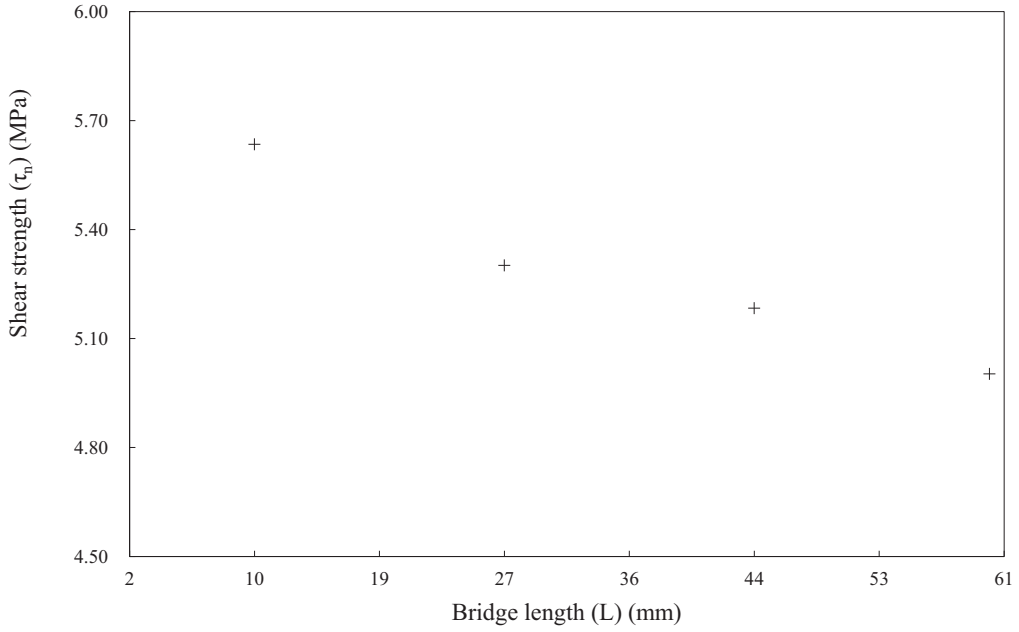

Fig. 25. Effect of L on τ_n obtained numerically from the shear loading on nonpersistent jointed rock.

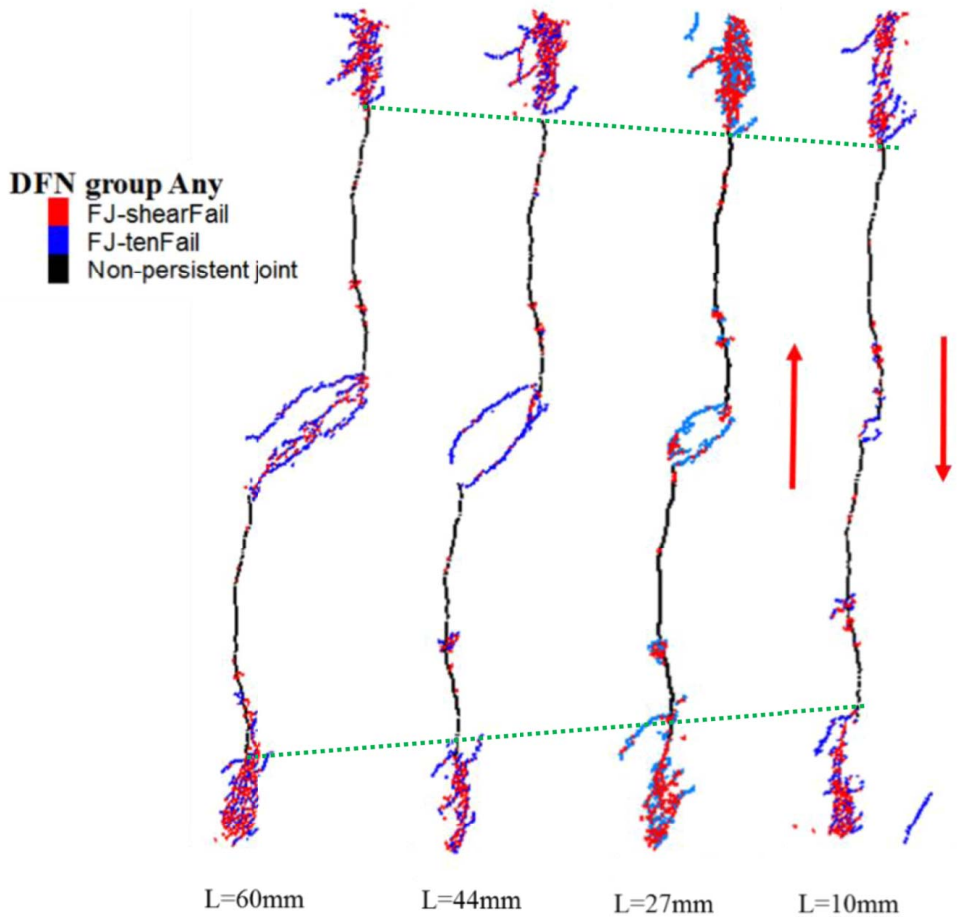

Fig. 26. Numerical simulations of cracking processes at different L under shearing.

the shear surfaces (the congregate of red cracks in Fig. 30). However, under a low σ_n, tensile cracking was the dominant mode where the crushed materials were not produced inside the shear surfaces.

Comparative Analysis

The previous sensitivity analyses compared the results under two main categories of uniaxial compression and shearing.

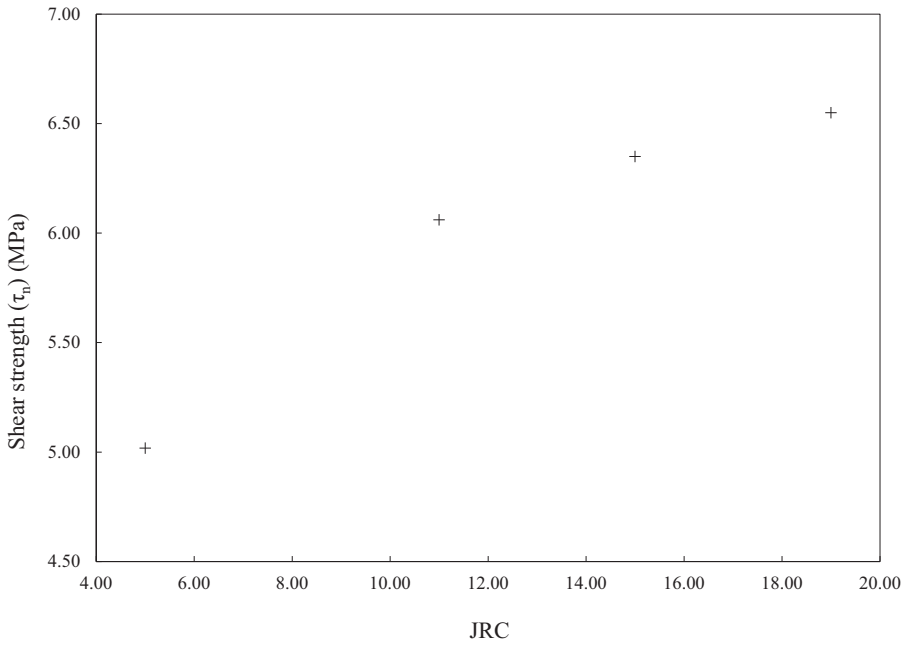

Fig. 27. Effect of JRC on τ_n obtained numerically from the shear loading on nonpersistent jointed rock.

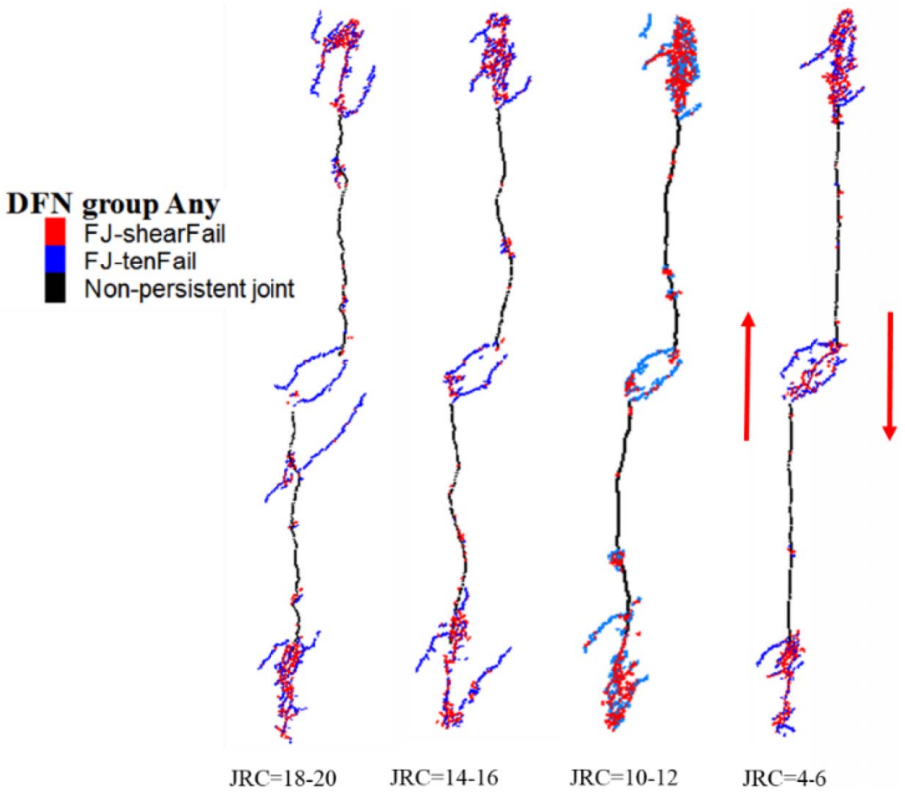

Fig. 28. Numerical simulations of cracking processes at different ranges of JRC under shearing.

The former included the variation in the parameters at four different levels, and the latter mainly consisted of the change in the parameters at four different levels. More stress levels could have been analyzed; however, in most conducted cases, the resulting trends were conclusive, and no further levels were performed.

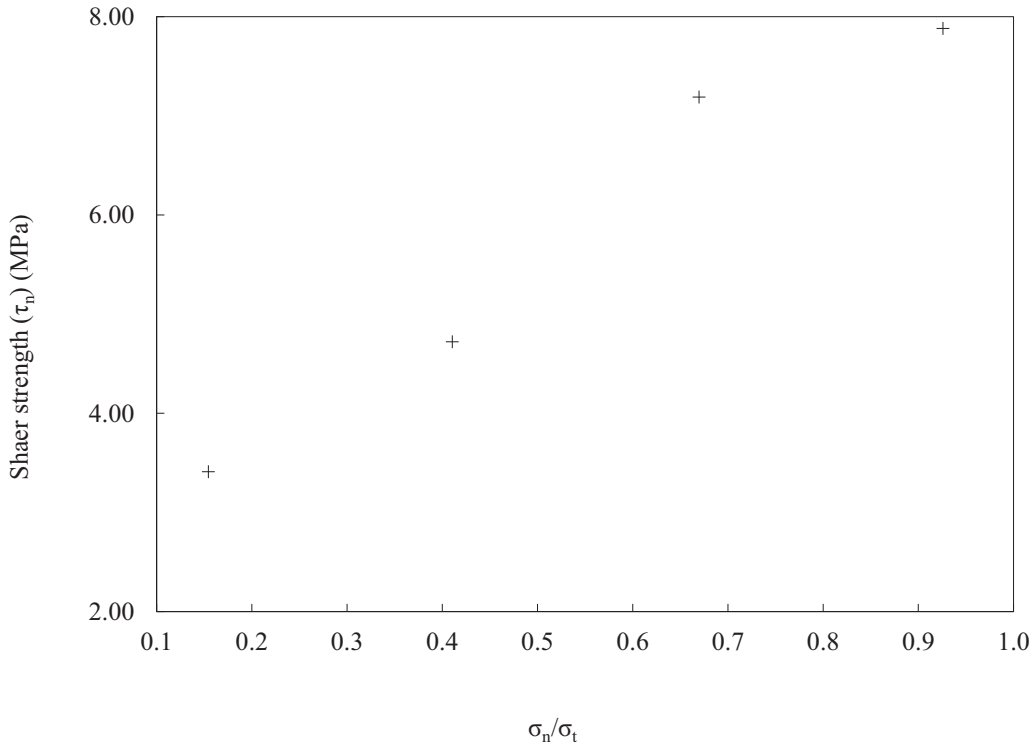

Fig. 29. Effect of σ_n on τ_n obtained numerically from the shear loading on nonpersistent jointed rock where σ_n were normalized by σ_t.

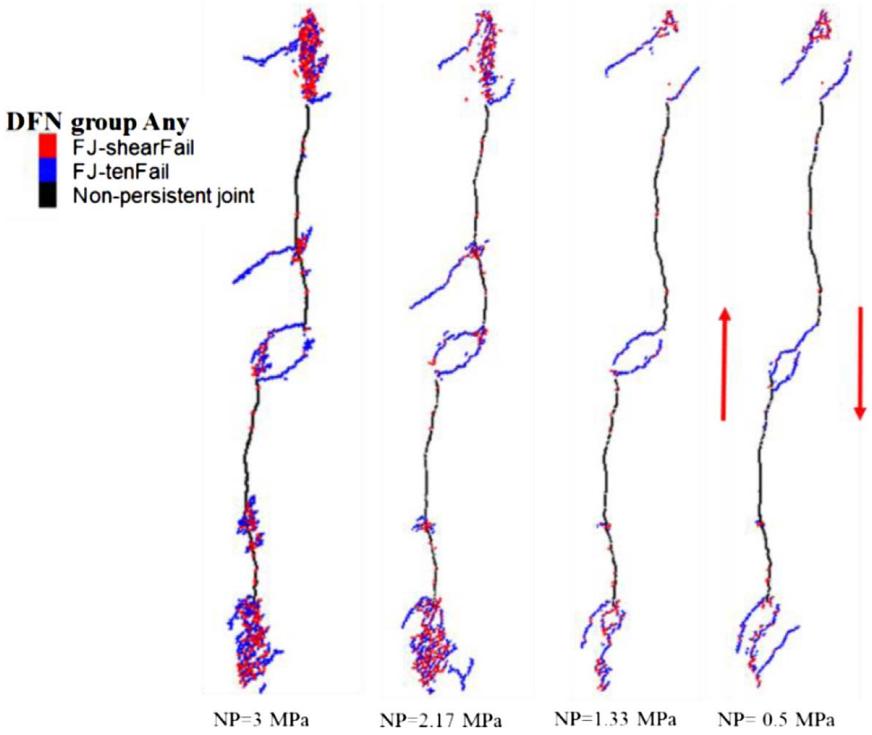

Fig. 30. Numerical simulations of cracking processes at different σ_n under shearing.

Discussion on the Numerical Results obtained from Uniaxial Compressive Loading

Numerical simulations under uniaxial compression demonstrated that other than θ, the remaining parameters caused an increase in the σ_{cm} and E_m of jointed rocks with linear correlations. However, θ exhibited descending trends for σ_{cm} and E_m to a certain angle, followed by the reverse correlations. Of note, for this particular parameter, the angle variation was from 0° to 90°, which was a complete range. Additional angles between 60° and 90° should be considered in future studies, which could shed light on the final trend in θ versus σ_{cm} and E_m in jointed rocks with rough joints.

Among JRC, γ, and L, the former was the most influential parameter that caused larger changes in the σ_{cm} and E_m. In addition, the change in L demonstrated that the variations in σ_{cm} and E_m between 10 and 30 mm were approximately linear; from 30 to 40 mm, they were quite different and nonlinear. Therefore, further investigations of this parameter at wider ranges are recommended for future analyses.

Discussion on the Numerical Results obtained from Shear Loading

From the numerical simulations under shearing, the JRC and σ_n directly correlated with τ_n, where an increase in these parameters led to an increase in τ_n. Figs. 27 and 29 show that the effect of σ_n on τ_n was higher than that by JRC within the defined levels in this study. This was endorsed by the cracking processes that resulted from both parameters shown in Figs. 28 and 30, where the resulting cracking processes of joints with JRC = 10–12 under a high σ_n were the same as that with the JRC = 18–20 under a low σ_n. Therefore, there was a balancing effect between JRC and σ_n under shearing.

In addition, L was the only parameter that exhibited a reverse correlation with τ_n, and γ demonstrated a fluctuating impact, which might be due to the outer ligaments. The L caused an approximate 20% reduction in τ_n in the range of 10–60 mm, and γ caused fluctuations in τ_n from approximately 25% to 30%. The cracking processes that resulted from both parameters revealed that γ mainly controlled the failure mode in the bridge area; the change in L did not significantly affect the cracking process.

Conclusions

The SRM technique in discrete element method was used to examine the effects of a number of important parameters on the uniaxial compressive and shear behaviors of jointed rocks with nonpersistent rough joints that included θ, γ, L, JRC, and σ_n. First, the numerical models were validated by the laboratory data reported by Asadizadeh et al. (2018b, 2019a), followed by sensitivity analysis.

Under uniaxial compressive loading, the resulting trends in σ_{cm} and E_m followed similar paths due to the change in the selected parameters. Other than θ, the remaining parameters that included γ, L, and JRC demonstrated almost direct correlations with σ_{cm} and E_m. The resulting trends from θ were descending and ascending for σ_{cm} and E_m, which might be due to the reduction in stress concentration at the joint tips that could lead to a uniform stress distribution across the bridge area.

Under shear loading, the impact of γ on τ_n led to a fluctuating trend where the initiation and propagation of wing cracks in the bridge area were responsible for the behavior, and the effect of L resulted in a descending trend where an increase in L led to a decrease in τ_n linearly. This descending trend might be due to the formation of wing tensile and shear cracks in which the wing cracks formed with an increase in L. After the development of tensile cracks, at larger L, the shear cracks were added to the wing cracks and led to a reduction in τ_n. Therefore, with an increase in the length of the central bridge, the outer ligament length decreased, which could result in the failure of a sample at a lower τ_n. The influence of JRC and σ_n on τ_n was directly proportional, where σ_n had

a greater impact than JRC. Such a mechanism could be associated with the formation of interlocking cracks, which were observed under shear loading where σ_n was changed from 0.5 to 3 MPa.

Data Availability Statement

All data, models, or codes that support the findings of this study are available from the corresponding author upon reasonable request.

References

Afolagboye, L. O., J. He, and S. Wang. 2017. "Experimental study on cracking behaviour of moulded gypsum containing two non-parallel overlapping flaws under uniaxial compression." *Acta Mech. Sin.* 33 (2): 394–405. https://doi.org/10.1007/s10409-016-0624-9.

Amadei, B., and R. E. Goodman. 1981. "A 3D constitutive relation for fractured rock masses." In *Proc., Int. Symp. Mechanical Behaviour of Structured Media*, 249–268. Ottawa: Elsevier Scientific.

Asadizadeh, M., M. F. Hossaini, M. Moosavi, H. Masoumi, and P. G. Ranjith. 2019a. "Mechanical characterisation of jointed rock-like material with non-persistent rough joints subjected to uniaxial compression." *Eng. Geol.* 260: 105224. https://doi.org/10.1016/j.enggeo.2019.105224.

Asadizadeh, M., H. Masoumi, H. Roshan, and A. Hedayat. 2019b. "Coupling Taguchi and response surface methodologies for the efficient characterization of jointed rocks" mechanical properties." *Rock Mech. Rock Eng.* 52 (11): 4807–4819. https://doi.org/10.1007/s00603-019-01853-1.

Asadizadeh, M., M. Moosavi, and M. F. Hossaini. 2018a. "Investigation of mechanical behaviour of non-persistent jointed blocks under uniaxial compression." *Geomech. Eng.* 14 (1): 29–42.

Asadizadeh, M., M. Moosavi, M. F. Hossaini, and H. Masoumi. 2018b. "Shear strength and cracking process of non-persistent jointed rocks: An extensive experimental investigation." *Rock Mech. Rock Eng.* 51 (2): 415–428. https://doi.org/10.1007/s00603-017-1328-6.

Bahaaddini, M. 2017. "Effect of boundary condition on the shear behaviour of rock joints in the direct shear test." *Rock Mech. Rock Eng.* 50: 1141–1155. https://doi.org/10.1007/s00603-016-1157-z.

Bahaaddini, M., P. Hagan, R. Mitra, and B. K. Hebblewhite. 2016a. "Numerical study of the mechanical behavior of nonpersistent jointed rock masses." *Int. J. Geomech.* 16 (1): 4015035. https://doi.org/10.1061/(ASCE)GM.1943-5622.0000510.

Bahaaddini, M., P. C. Hagan, R. Mitra, and B. K. Hebblewhite. 2014a. "Scale effect on the shear behaviour of rock joints based on a numerical study." *Eng. Geol.* 181: 212–223. https://doi.org/10.1016/j.enggeo.2014.07.018.

Bahaaddini, M., P. C. Hagan, R. Mitra, and B. K. Hebblewhite. 2015. "Parametric study of smooth joint parameters on the shear behaviour of rock joints." *Rock Mech. Rock Eng.* 48 (3): 923–940. https://doi.org/10.1007/s00603-014-0641-6.

Bahaaddini, M., P. C. Hagan, R. Mitra, and M. H. Khosravi. 2016b. "Experimental and numerical study of asperity degradation in the direct shear test." *Eng. Geol.* 204: 41–52. https://doi.org/10.1016/J.ENGGEO.2016.01.018.

Bahaaddini, M., J. Saymontry, H. Masoumi, and P. Hagan. 2014b. "Experimental study of the shear behavior of rock joints under constant normal load and constant normal stiffness conditions." In *Proc., 48th U.S. Rock Mechanics/Geomechanics Symp.*, 1650–1656. Alexandria, VA: American Rock Mechanics Association (ARMA).

Bahaaddini, M., G. Sharrock, and B. K. Hebblewhite. 2013a. "Numerical direct shear tests to model the shear behaviour of rock joints." *Comput. Geotech.* 51: 101–115. https://doi.org/10.1016/j.compgeo.2013.02.003.

Bahaaddini, M., G. Sharrock, and B. K. Hebblewhite. 2013b. "Numerical investigation of the effect of joint geometrical parameters on the mechanical properties of a non-persistent jointed rock mass under uniaxial compression." *Comput. Geotech.* 49: 206–225. https://doi.org/10.1016/j.compgeo.2012.10.012.

Bahaaddini, M., G. Sharrock, B. K. Hebblewhite, and R. Mitra. 2012. "Statistical analysis of the effect of joint geometrical parameters on the mechanical properties of non-persistent jointed rock masses." In *Proc., 46th US Rock Mechanics/GeoMechanics Symp.*, 2778–2786. Alexandria, VA: American Rock Mechanics Association (ARMA).

Bandis, S. C., A. C. Lumsden, and N. R. Barton. 1983. "Fundamentals of rock joint deformation." *Int. J. Rock Mech. Min. Sci. Geomech. Abstr.* 20 (6): 249–268. https://doi.org/10.1016/0148-9062(83)90595-8.

Barton, N. 1976. "The shear strength of rock and rock joints." *Int. J. Rock Mech. Min. Sci. Geomech. Abstr.* 13 (9): 255–279. https://doi.org/10.1016/0148-9062(76)90003-6.

Bieniawski, Z. T., and I. Hawkes. 1978. "Suggested methods for determining tensile strength of rock materials." *Int. J. Rock Mech. Min. Sci. Geomech. Abstr.* 15 (3): 99–103. https://doi.org/10.1016/0148-9062(78)90003-7.

Bobet, A. 2000. "The initiation of secondary cracks in compression." *Eng. Fract. Mech.* 66 (2): 187–219. https://doi.org/10.1016/S0013-7944(00)00009-6.

Bobet, A., and H. H. Einstein. 1998. "Fracture coalescence in rock-type materials under uniaxial and biaxial compression." *Int. J. Rock Mech. Min. Sci.* 35 (7): 863–888. https://doi.org/10.1016/S0148-9062(98)00005-9.

Brady, B. H. G., and E. T. Brown. 2004. "Rock mechanics for underground mining." In *Rock mechanics: For underground mining*, 3rd ed. Dordrecht, Netherlands: Springer.

Brown, E. T., and D. H. Trollope. 1970. "Strength of a model of jointed rock." *J. Soil Mech. Found. Div.* 96 (2): 685–704. https://doi.org/10.1061/JSFEAQ.0001411.

Cao, P., T. Liu, C. Pu, and H. Lin. 2015. "Crack propagation and coalescence of brittle rock-like specimens with pre-existing cracks in compression." *Eng. Geol.* 187: 113–121. https://doi.org/10.1016/j.enggeo.2014.12.010.

Cao, R.-h., P. Cao, H. Lin, C.-z. Pu, and K. Ou. 2016. "Mechanical behavior of brittle rock-like specimens with pre-existing fissures under uniaxial loading: Experimental studies and particle mechanics approach." *Rock Mech. Rock Eng.* 49 (3): 763–783. https://doi.org/10.1007/s00603-015-0779-x.

Cao, R. H., P. Cao, H. Lin, G. W. Ma, X. Fan, and X. G. Xiong. 2018. "Mechanical behavior of an opening in a jointed rock-like specimen under uniaxial loading: Experimental studies and particle mechanics approach." *Arch. Civ. Mech. Eng.* 18: 198214. https://doi.org/10.1016/j.acme.2017.06.010.

Cao, R., R. Yao, J. J. Meng, Q. Lin, H. Lin, and S. Li. 2020. "Failure mechanism of non-persistent jointed rock-like specimens under uniaxial loading: Laboratory testing." *Int. J. Rock Mech. Min. Sci.* 132 (April). 104341. https://doi.org/10.1016/j.ijrmms.2020.104341.

Chang, L., H. Konietzky, and T. Frühwirt. 2019. "Strength anisotropy of rock with crossing joints: Results of physical and numerical modeling with gypsum models." *Rock Mech. Rock Eng.* 52 (7): 2293–2317. https://doi.org/10.1007/s00603-018-1714-8.

Cheng, C., X. Chen, and S. Zhang. 2016a. "Multi-peak deformation behavior of jointed rock mass under uniaxial compression: Insight from particle flow modeling." *Eng. Geol.* 213: 25–45. https://doi.org/10.1016/j.enggeo.2016.08.010.

Cheng, H., X. Zhou, J. Zhu, and Q. Qian. 2016b. "The effects of crack openings on crack initiation, propagation and coalescence behavior in rock-like materials under uniaxial compression." *Rock Mech. Rock Eng.* 49 (9): 3481–3494. https://doi.org/10.1007/s00603-016-0998-9.

Dershowitz, W. S., and H. H. Einstein. 1988. "Characterizing rock joint geometry with joint system models." *Rock Mech. Rock Eng.* 21: 21–51. https://doi.org/10.1007/BF01019674.

Einstein, H. H., and R. C. Hirschfeld. 1973. "Model studies on mechanics of jointed rock." *J. Soil Mech. Found. Div.* 99 (3): 229–248. https://doi.org/10.1061/JSFEAQ.0001859.

Einstein, H. H., R. C. Hirschfeld, R. A. Nelson, and R. W. Bruhn. 1969. "Model studies of jointed-rock behavior." In *Proc., 11th US Symp. Rock Mech.* New York: American Institute of Mining, Metallurgical, and Petroleum Engineers Inc.

Fereshtenejad, S., J. Kim, and J.-J. Song. 2021a. "Experimental study on shear mechanism of rock-like material containing a single non-persistent rough joint." *Energies* 14 (4): 987. https://doi.org/10.3390/en14040987.

Fereshtenejad, S., J. Kim, and J.-J. Song. 2021b. "Empirical model for shear strength of artificial rock containing a single nonpersistent joint." *Int. J. Geomech.* 21 (8): 04021123. https://doi.org/10.1061/(ASCE)GM.1943-5622.0002099.

Gehle, C., and H. K. Kutter. 2003. "Breakage and shear behaviour of intermittent rock joints." *Int. J. Rock Mech. Min. Sci.* 40 (5): 687–700. https://doi.org/10.1016/S1365-1609(03)00060-1.

Ghazvinian, A., V. Sarfarazi, W. Schubert, and M. Blumel. 2012. "A study of the failure mechanism of planar non-persistent open joints using PFC2D." *Rock Mech. Rock Eng.* 45 (5): 677–693.

Goldstein, M., B. Goosev, N. Pvrogovsky, R. Tulinov, and A. Turovskaya. 1966. "Investigation of mechanical properties of cracked rock." In *Proc., 1st Congress Int. Society for Rock Mechanics*. Lisbon, Portugal: National Laboratory of Civil Engineering.

Grasselli, G. 2006. "Manuel Rocha medal recipient shear strength of rock joints based on quantified surface description." *Rock Mech. Rock Eng.* 39 (4): 295–314. https://doi.org/10.1007/s00603-006-0100-0.

Guo, J., P. Liu, S. Huang, Y. Qian, and G. Liu. 2020. "Cracking processes and failure modes of rock-like specimens with a set of non-persistent joints." *Geotech. Geol. Eng.* 3 (39): 1237–1257.

Huang, C., W. Yang, K. Duan, L. Fang, L. Wang, and C. Bo. 2019. "Mechanical behaviors of the brittle rock-like specimens with multi-non-persistent joints under uniaxial compression." *Constr. Build. Mater.* 220: 426–443. https://doi.org/10.1016/j.conbuildmat.2019.05.159.

Huang, Y.-H., S.-Q. Yang, W.-L. Tian, W. Zeng, and L.-Y. Yu. 2016. "An experimental study on fracture mechanical behavior of rock-like materials containing two unparallel fissures under uniaxial compression." *Acta Mech. Sin.* 32 (3): 442–455. https://doi.org/10.1007/s10409-015-0489-3.

Itasca Consulting Group. 2022. *PFC2D manual*. Minneapolis: Itasca.

Ivars, D. M., et al. 2011. "The synthetic rock mass approach for jointed rock mass modelling." *Int. J. Rock Mech. Min. Sci.* 48 (2): 219–244. https://doi.org/10.1016/j.ijrmms.2010.11.014.

Jade, S., and T. G. Sitharam. 2003. "Characterization of strength and deformation of jointed rock mass based on statistical analysis." *Int. J. Geomech.* 3 (1): 43–54. https://doi.org/10.1061/(ASCE)1532-3641(2003)3:1(43).

Korinets, A., and H. Alehossein. 2002. "Technical note On the initial Non-linearity of compressive stress-strain curves for intact rock." *Rock Mech. Rock Eng.* 35 (4): 319–328. https://doi.org/10.1007/s00603-002-0030-4.

Kovari, K., A. Tisa, H. H. Einstein, and J. A. Franklin. 1983. "Suggested methods for determining the strength of rock materials in triaxial compression: Revised version." *Int. J. Rock Mech. Min. Sci.* 20 (6): 283–290.

Lajtai, E. Z. 1969. "Shear strength of weakness planes in rock." *Int. J. Rock Mech. Min. Sci. Geomech. Abstr.* 6 (5): 499–515. https://doi.org/10.1016/0148-9062(69)90016-3.

Lee, H., and S. Jeon. 2011. "An experimental and numerical study of fracture coalescence in pre-cracked specimens under uniaxial compression." *Int. J. Solids Struct.* 48 (6): 979–999. https://doi.org/10.1016/j.ijsolstr.2010.12.001.

Ma, C., W. Yao, Y. Yao, and J. Li. 2018. "Simulating strength parameters and size effect of stochastic jointed rock mass using DEM method." *KSCE J. Civ. Eng.* 22 (12): 4872–4881. https://doi.org/10.1007/s12205-017-1581-y.

Mehrdad, I., H. R. Nejati, K. Goshtasbi, and A. Nazerigivi. 2022. "Effect of brittleness on the micromechanical damage and failure pattern of rock specimens." *Smart Struct. Syst.* 29 (4): 535–547. https://doi.org/10.12989/SSS.2022.29.4.535.

Muralha, J., G. Grasselli, B. Tatone, M. Blümel, P. Chryssanthakis, and J. Yujing. 2014. "ISRM suggested method for laboratory determination of the shear strength of rock joints: Revised version." *Rock Mech. Rock Eng.* 47 (1): 291–302. https://doi.org/10.1007/s00603-013-0519-z.

Park, C. H., and A. Bobet. 2009. "Crack coalescence in specimens with open and closed flaws: A comparison." *Int. J. Rock Mech. Min. Sci.* 46 (5): 819–829. https://doi.org/10.1016/j.ijrmms.2009.02.006.

Park, C. H., and A. Bobet. 2010. "Crack initiation, propagation and coalescence from frictional flaws in uniaxial compression." *Eng. Fract. Mech.* 77 (14): 2727–2748. https://doi.org/10.1016/j.engfracmech.2010.06.027.

Park, J.-W., and J.-J. Song. 2009. "Numerical simulation of a direct shear test on a rock joint using a bonded-particle model." *Int. J. Rock Mech. Min. Sci.* 46 (8): 1315–1328. https://doi.org/10.1016/j.ijrmms.2009.03.007.

Patton, F. D. 1966. "Multiple modes of shear failure in rock." In *Proc., 1st Congress Int. Society for Rock Mechanics*, 509–513. Lisbon, Portugal: International Society for Rock Mechanics and Rock Engineering.

Pierce, M., P. Cundall, D. Potyondy, and D. Mas Ivars. 2007. "A synthetic rock mass model for jointed rock." In *Proc., 1st CA–US Rock Mech. Symp.*, 341–349. Alexandria, VA: American Rock Mechanics Association (ARMA).

Potyondy, D. O. 2012. "A flat-jointed bonded-particle material for hard rock." In *Proc., 46th US Rock Mech. Symp*. Alexandria, VA: American Rock Mechanics Association (ARMA).

Potyondy, D. O., and P. A. Cundall. 2004. "A bonded-particle model for rock." *Int. J. Rock Mech. Min. Sci.* 41 (8): 1329–1364. https://doi.org/10.1016/j.ijrmms.2004.09.011.

Prudencio, M., and M. Van Sint Jan. 2007. "Strength and failure modes of rock mass models with non-persistent joints." *Int. J. Rock Mech. Min. Sci.* 44 (6): 890–902. https://doi.org/10.1016/j.ijrmms.2007.01.005.

Saeb, S., and B. Amadei. 1992. "Modelling rock joints under shear and normal loading." *Int. J. Rock Mech. Min. Sci. Geomech. Abstr.* 29: 267–278. https://doi.org/10.1016/0148-9062(92)93660-C.

Sagong, M., and A. Bobet. 2002. "Coalescence of multiple flaws in a rock-model material in uniaxial compression." *Int. J. Rock Mech. Min. Sci.* 39 (2): 229–241. https://doi.org/10.1016/S1365-1609(02)00027-8.

Sarfarazi, V., A. Ghazvinian, W. Schubert, M. Blumel, and H. R. Nejati. 2014. "Numerical simulation of the process of fracture of echelon rock joints." *Rock Mech. Rock Eng.* 47 (4): 1355–1371. https://doi.org/10.1007/s00603-013-0450-3.

Sarfarazi, V., H. Haeri, A. B. Shemirani, and Z. Zhu. 2017. "Shear behavior of non-persistent joint under high normal load." *Strength Mater.* 49 (2): 320–334. https://doi.org/10.1007/s11223-017-9872-6.

Shaunik, D., and M. Singh. 2019. "Strength behaviour of a model rock intersected by non-persistent joint." *J. Rock Mech. Geotech. Eng.* 11 (6): 1243–1255. https://doi.org/10.1016/j.jrmge.2019.01.004.

Singh, M., K. S. Rao, and T. Ramamurthy. 2002. "Strength and deformational behaviour of a jointed rock mass." *Rock Mech. Rock Eng.* 35 (1): 45–64. https://doi.org/10.1007/s006030200008.

Singh, M., and B. Singh. 2008. "High lateral strain ratio in jointed rock masses." *Eng. Geol.* 98 (3–4): 75–85. https://doi.org/10.1016/j.enggeo.2007.11.004.

Tang, C. A., P. Lin, R. H. C. Wong, and K. T. Chau. 2001. "Analysis of crack coalescence in rock-like materials containing three flaws—part II: Numerical approach." *Int. J. Rock Mech. Min. Sci.* 38 (7): 925–939. https://doi.org/10.1016/S1365-1609(01)00065-X.

Wang, P., F. Ren, S. Miao, M. Cai, and T. Yang. 2017. "Evaluation of the anisotropy and directionality of a jointed rock mass under numerical direct shear tests." *Eng. Geol.* 225: 29–41. https://doi.org/10.1016/j.enggeo.2017.03.004.

Wang L.-y., W. z. Chen, X. y. Tan, X.-j. Tan, J.-q. Yuan and Q. Liu. 2019. "Evaluation of mountain slope stability considering the impact of geological interfaces using discrete fractures model." *J. Mt. Sci.* 16: 21842202. https://doi.org/10.1007/s11629-019-5527-3.

Wittke, W. 2014. *Rock mechanics based on an anisotropic jointed rock model*. Berlin: Wilhelm Ernst & Sohn.

Wong, L. N. Y., and H. H. Einstein. 2009. "Crack coalescence in molded gypsum and Carrara marble: Part 1. Macroscopic observations and interpretation." *Rock Mech. Rock Eng.* 42 (3): 475–511. https://doi.org/10.1007/s00603-008-0002-4.

Wong, R. H. C., and K. T. Chau. 1998. "Crack coalescence in a rock-like material containing two cracks." *Int. J. Rock Mech. Min. Sci.* 35 (2): 147–164. https://doi.org/10.1016/S0148-9062(97)00303-3.

Xiong, L., H. Chen, X. Geng, and Z. Xu. 2020a. "Influence of joint location and connectivity on the shear properties of artificial rock samples with non-persistent planar joints." *Arabian J. Geosci.* 13 (13): 565. https://doi.org/10.1007/s12517-020-05589-z.

Xiong, L., H. Chen, and Y. Zhang. 2020b. "Direct shear tests of artificial jointed rock specimens with parallel joints." *Arabian J. Geosci.* 13 (10): 373. https://doi.org/10.1007/s12517-020-05424-5.

Yang, S.-Q., M. Chen, Y.-H. Huang, H.-W. Jing, and P. G. Ranjith. 2020. "An experimental study on fracture evolution mechanism of a non-persistent jointed rock mass with various anchorage effects by DSCM, AE and X-ray CT observations." *Int. J. Rock Mech. Min. Sci.* 134 (September): 104469. https://doi.org/10.1016/j.ijrmms.2020.104469.

Yang, X.-X., and W.-G. Qiao. 2018. "Numerical investigation of the shear behavior of granite materials containing discontinuous joints by utilizing the flat-joint model." *Comput. Geotech.* 104 (August): 69–80. https://doi.org/10.1016/j.compgeo.2018.08.014.

Zare, S., S. Karimi-Nasab, and H. Jalalifar. 2021. "Analysis and determination of the behavioral mechanism of rock bridges using experimental and numerical modeling of non-persistent rock joints." *Int. J. Rock Mech. Min. Sci.* 141 (September 2020): 104714. https://doi.org/10.1016/j.ijrmms.2021.104714.

Zhang, X.-P., and L. N. Y. Wong. 2013. "Crack initiation, propagation and coalescence in rock-like material containing two flaws: A numerical study based on bonded-particle model approach." *Rock Mech. Rock Eng.* 46 (5): 1001–1021. https://doi.org/10.1007/s00603-012-0323-1.

Zhang, Z.-l., and T. Wang. 2020. "Numerical analysis of loess and weak intercalated layer failure behavior under direct shearing and cyclic loading." *J. Mountain Sci.* 17 (11): 2796–2815. https://doi.org/10.1007/s11629-020-6178-0.

Zhao, Y., S. Liu, Y. Jiang, K. Wang, and Y. Huang. 2016. "Dynamic tensile strength of coal under dry and saturated conditions." *Rock Mech. Rock Eng.* 49 (5): 1709–1720. https://doi.org/10.1007/s00603-015-0849-0.

Zhou X., and J. Chen. 2019. "Extended finite element simulation of step-path brittle failure in rock slopes with non-persistent en-echelon joints." *Eng. Geol.* 250: 6588. https://doi.org/10.1016/j.enggeo.2019.01.012.

Zhou, X. P., H. Cheng, and Y. F. Feng. 2014. "An experimental study of crack coalescence behavior in rock-like materials containing multiple flaws under uniaxial compression." *Rock Mech. Rock Eng.* 47 (6): 1961–1986. https://doi.org/10.1007/s00603-013-0511-7.